

# Locally-Adaptive Bayesian Nonparametric Inference for Phylodynamics

James R. Faulkner<sup>1,2</sup>, Andrew F. Magee<sup>3</sup>, Beth Shapiro<sup>4</sup>, Vladimir N. Minin<sup>5,\*</sup>

<sup>1</sup>*Quantitative Ecology and Resource Management, University of Washington, Seattle, WA, U.S.A.*

<sup>2</sup>*National Marine Fisheries Service, Northwest Fisheries Science Center, Seattle, WA, U.S.A.*

<sup>3</sup>*Department of Biology, University of Washington, Seattle, WA, U.S.A.*

<sup>4</sup>*Ecology and Evolutionary Biology Department and Genomics Institute,  
University of California, Santa Cruz, CA., U.S.A.*

<sup>5</sup>*Department of Statistics, University of California, Irvine, CA, U.S.A.*

\*Corresponding author: [vminin@uci.edu](mailto:vminin@uci.edu)

## Abstract

Phylodynamics is an area of population genetics that uses genetic sequence data to estimate past population dynamics. Modern state-of-the-art Bayesian nonparametric methods for phylodynamics use either change-point models or Gaussian process priors to recover population size trajectories of unknown form. Change-point models suffer from computational issues when the number of change-points is unknown and needs to be estimated. Gaussian process-based methods lack local adaptivity and cannot accurately recover trajectories that exhibit features such as abrupt changes in trend or varying levels of smoothness. We propose a novel, locally-adaptive approach to Bayesian nonparametric phylodynamic inference that has the flexibility to accommodate a large class of functional behaviors. Local adaptivity results from modeling the log-transformed effective population size *a priori* as a horseshoe Markov random field, a recently proposed statistical model that blends together the best properties of the change-point and Gaussian process modeling paradigms. We use simulated data to assess model performance, and find that our proposed method results in reduced bias and increased precision when compared to contemporary methods. We also use our models to reconstruct past changes in genetic diversity of human hepatitis C virus in Egypt and to estimate population size changes of ancient and modern steppe bison. These analyses show that our new method captures features of the population size trajectories that were missed by the state-of-the-art phylodynamic methods.

## 1 Introduction

Estimation of population sizes and population dynamics over time is an important task in ecology and epidemiology. Census population sizes can be difficult to estimate due to infeasible sampling requirements or study costs. Genetic sequences are a growing source of information that can be used to infer past population sizes from the signatures of genetic diversity. Phylodynamics is a discipline that uses genetic sequence data to estimate past population dynamics. Many phylodynamic models draw on coalescent theory (Kingman, 1982; Griffiths and Tavaré, 1994), which provides a probabilistic framework that connects the branching times of

a genealogical tree with the effective size and other demographic variables, such as migration rates, of the population from which the genealogy was drawn. Effective population size can be interpreted as a measure of genetic diversity in a population and is proportional to census population size if coalescent model assumptions are met. When genetic diversity is high, the effective population size approaches the census population size, given random mating and no inbreeding or genetic drift, but is otherwise smaller than the census size. In our work we concentrate on estimation of effective population sizes over evolutionary time, which can be short for rapidly evolving virus populations and longer (but still estimable with preserved ancient molecular sequence samples) for more slowly-evolving organisms. Some examples of successful application of phylodynamics include describing seasonal trends of influenza virus spread around the world (Rambaut et al., 2008), quantifying dynamics of outbreaks like hepatitis C (Pybus et al., 2003) and Ebola viruses (Alizon et al., 2014; Volz and Pond, 2014), and assessing the effects of climate change on populations of large mammals during the ice ages using ancient DNA (Shapiro et al., 2004; Lorenzen et al., 2011).

Some approaches to phylodynamics use parametric functional relationships to describe effective population size trajectories (*e.g.*, Pybus et al., 2003; Rasmussen et al., 2014), but nonparametric methods offer a flexible alternative when an accurate estimate of a complex population size trajectory is needed and knowledge of the mechanisms driving population size changes is incomplete. Nonparametric models have a long history of use in phylodynamics. Pybus et al. (2000) introduced a nonparametric method, called the skyline plot, that produced point-wise estimates of population size, where the number of estimates was equal to the number of sampled genetic sequences minus one. The estimates from this method were highly variable, so a modification, referred to as the generalized skyline plot, created a set of discrete time interval groups that shared a single effective population size (Strimmer and Pybus, 2001). These likelihood-based approaches were adapted to a Bayesian framework with the Bayesian skyline plot (Drummond et al., 2005) and the variable-knot spline approach of Opgen-Rhein et al. (2005). Minin et al. (2008) provided an alternative to these change-point methods by introducing a Gaussian Markov random field (GMRF) smoothing prior that connected the piecewise-constant population size estimates between coalescent events without needing to specify or estimate knot locations. Palacios and Minin (2012) and Gill et al. (2013) extended the GMRF approach of Minin et al. (2008) by constructing a GMRF prior on a discrete uniform grid. A grid-free approach, introduced by Palacios and Minin (2013), allowed the population size trajectories to vary continuously by using a Gaussian process (GP) prior.

Modern nonparametric Bayesian methods for phylodynamics offer the state-of-the-art for recovering effective population size trajectories of unknown form. However, current methods cannot accurately recover trajectories that exhibit challenging features such as abrupt changes or varying levels of smoothness. Such features may arise in populations in the form of bottlenecks, rapid population changes, or aperiodic fluctuations with varying amplitudes. Accurate estimation of features like these can be important for understanding the demographic history of a population. Outside of phylodynamics, various nonparametric statistical methods have been developed to deal with such nonstationary or locally-varying behavior under more standard likelihoods. These methods include, but are not limited to, GPs with nonstationary covariance functions (Paciorek and Schervish, 2006), nonstationary process convolutions (Higdon, 1998; Fuentes, 2002), non-Gaussian Matérn fields (Wallin and Bolin, 2015), and adaptive smoothing splines (Yue et al., 2012, 2014). Each of these methods has good qualities and could potentially be adapted for phylodynamics, but methods based on continuous random fields or process convolutions can be computationally challenging for large data sets, and some spline methods require selection or modeling of the number and location of knots.

A recent method by Faulkner and Minin (2018) uses shrinkage priors in combination with Markov random fields to perform nonparametric smoothing with locally-adaptive properties. This is a fully Bayesian method that does not require the use of knots and avoids the costly computations of inverting dense covariance matrices. Computations instead take advantage of the sparsity in the precision matrix of the Markov random field to avoid matrix inversion. Faulkner and Minin (2018) compared different specifications of their shrinkage prior Markov random field (SPMRF) models and found that putting a horseshoe prior on the  $k$ th order differences between successive function values had superior performance when applied to underlying functions with sharp breaks or varying levels of smoothness. We refer to the model with the horseshoe prior as a horseshoe Markov random field (HSMRF).

In this paper, we propose an adaptation of the HSMRF approach of Faulkner and Minin (2018) for use in phylodynamic inference. We describe the first application of the HSMRF prior to the coalescent model and devise a new MCMC scheme for the model that uses efficient, tuning-parameter-free, high-dimensional block updates. We provide an implementation of this MCMC in the program RevBayes, which allows us to target the joint distribution of genealogy, evolutionary model parameters, and effective population size parameters. We also develop a method for setting the hyperparameter on the prior for the global shrinkage parameter for coalescent data. We use simulations to compare the performance of the HSMRF model to that of a GMRF model and show that our model has lower bias and higher precision across a set of population trajectories that are difficult to estimate. We then apply our model to two real data examples that are well-known in the phylodynamics literature and compare its performance to other popular nonparametric methods. The first example reanalyzes epidemiological dynamics of hepatitis C virus in Egypt and the second looks at estimation of ancient bison population size changes from DNA data.

## 2 Methods

### 2.1 Sequence Data and Substitution Model

Suppose we have a set of  $n$  aligned RNA or DNA sequences for a set of  $L$  sites within a gene. We assume the sequences come from a random sample of  $n$  individuals from a well-mixed population, where samples were collected potentially at different times. Let  $\mathbf{Y}$  be the  $n \times L$  sequence alignment matrix. We assume the sites are fully linked with no recombination possible between the sequences. This allows us to assume the existence of a genealogy  $\mathbf{g}$ , which is a rooted bifurcating tree that describes the ancestral relationships among the sampled individuals.

We assume that  $\mathbf{Y}$  is generated by a continuous time Markov chain (CTMC) substitution model that models the evolution of the discrete states (*e.g.*, A,C,T,G for DNA) along the genealogy  $\mathbf{g}$  for each alignment site. A variety of substitution models are available and are typically differentiated by the form of the transition matrix  $M(\mathbf{\Omega})$ , which controls the substitution rates in the CTMC for the nucleotide bases with a set of parameters  $\mathbf{\Omega}$  (see Yang (2014) for examples). The likelihood of the sequence data given the genealogy and substitution parameters can be written  $p(\mathbf{Y} | \mathbf{g}, \mathbf{\Omega})$ . This is often referred to as the Felsenstien likelihood and can be efficiently computed using Felsenstien’s pruning algorithm (Felsenstein, 1981).

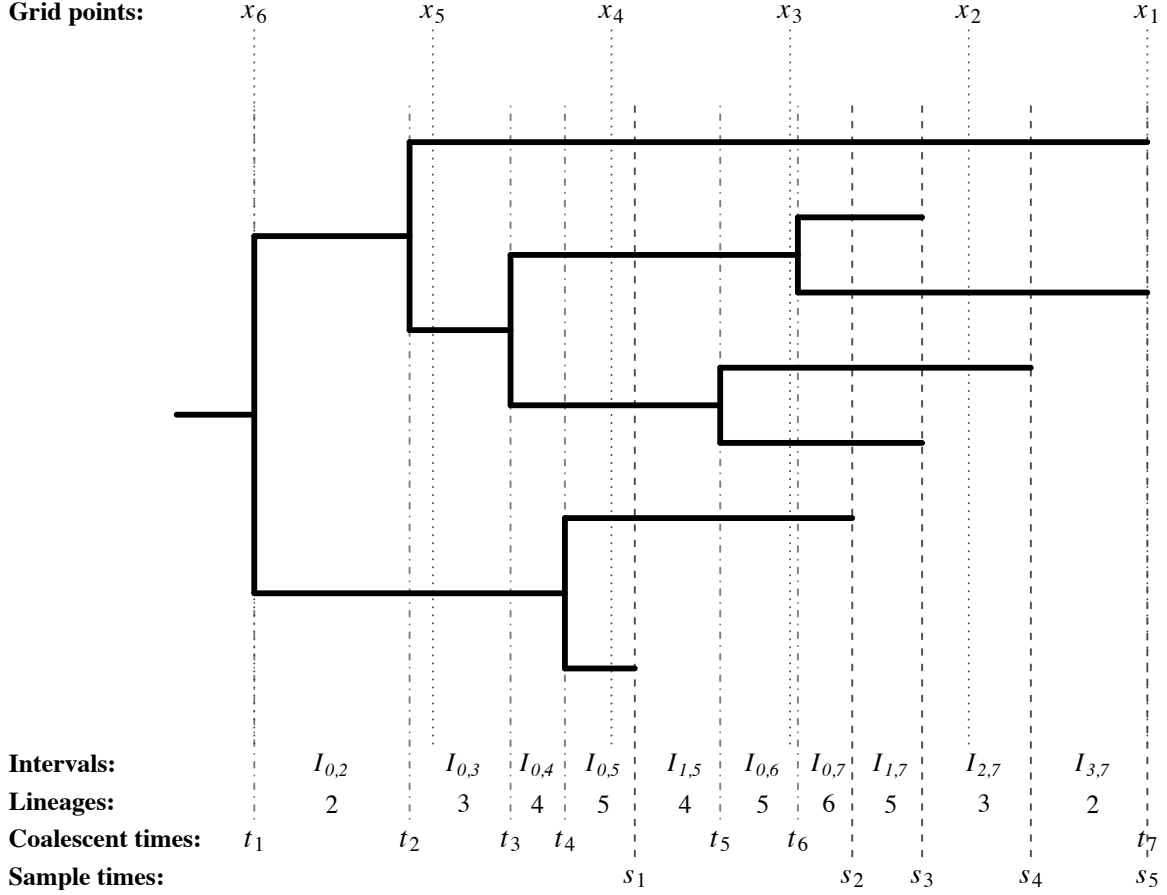


Figure 1: Genealogical tree under heterochronous sampling showing the relationship between sampling times  $s_i$ , coalescent times  $t_i$ , intervals  $I_{i,k}$ , number of lineages  $n_{i,k}$ , and the uniform grid points,  $x_h$ , used for approximating coalescent densities.

## 2.2 Coalescent

Suppose that we now have a genealogy  $\mathbf{g}$ , where branch lengths of the genealogical tree are measured in units of clock time (*e.g.*, years). To build a Bayesian hierarchical model, we need a prior density for  $\mathbf{g}$ . The times at which two lineages merge into a common ancestor on the tree are called coalescent times. The coalescent model provides a probabilistic framework for relating the coalescent times in the sample to the effective size of the population. Kingman (1982) developed the coalescent model for a constant effective population size and Griffiths and Tavaré (1994) extended it for varying effective population sizes.

Let the coalescent times arising from genealogy  $\mathbf{g}$  be denoted  $t_n = 0 < t_{n-1} < \dots < t_1$ , where 0 is the present and time is measured backward from there. We will assume the general case where sampling of the genetic sequences occurs at different times (*heterochronous sampling*), which will include the special case where all sampling occurs at a single time point  $t_n = 0$  (*isochronous sampling*). We denote the set of sampling times as  $s_m = 0 < s_{m-1} < \dots < s_1 < t_1$  for samples of size  $n_m, \dots, n_1$ , respectively, where  $n = \sum_{j=1}^m n_j$  (Figure 1). We let  $\mathbf{s}$  denote the vector of sampling times. Further, we let the intervals that end with a coalescent event be denoted  $I_{0,k} = (\max\{t_k, s_j\}, t_{k-1}]$ , for  $s_j < t_{k-1}$  and  $k = 2, \dots, n$ , and let the intervals that end with a sampling event be denoted  $I_{i,k} = (\max\{t_k, s_{j+i}\}, s_{j+i-1}]$ , for  $s_{j+i-1} > t_k$  and  $s_j < t_{k-1}$ ,  $k =$

$2, \dots, n$ . If we let  $n_{i,k}$  be the number of lineages present in interval  $I_{i,k}$  and let the vector of number of lineages be denoted  $\mathbf{n}$ , then the joint density of the coalescent times given  $\mathbf{s}$  and  $N_e(t)$  can be written as

$$\begin{aligned} p(t_1, t_2, \dots, t_{n-1} \mid \mathbf{s}, \mathbf{n}, N_e(t)) &= \prod_{k=2}^n p(t_{k-1} \mid t_k, \mathbf{s}, \mathbf{n}, N_e(t)) \\ &= \prod_{k=2}^n \frac{C_{0,k}}{N_e(t_{k-1})} \exp \left\{ - \sum_{i=0}^m \int_{I_{i,k}} \frac{C_{i,k}}{N_e(t)} dt \right\}, \end{aligned} \quad (1)$$

where  $C_{i,k} = \binom{n_{i,k}}{2}$  is the coalescent factor (Felsenstein and Rodrigo, 1999). This model can be seen as an inhomogeneous Markov point process where the conditional intensity is  $C_{i,k}[N_e(t)]^{-1}$  (Palacios and Minin, 2013).

The integrals in equation (1) are computationally intractable since  $N_e(t)$  is an unknown infinite-dimensional parameter. However, following Palacios and Minin (2012), Gill et al. (2013), and Lan et al. (2015) we can use an approximation over a finite grid to make the computations tractable. We construct a regular grid,  $\mathbf{x} = \{x_h\}_{h=1}^H$ , and set the end points of the grid  $\mathbf{x}$  such that  $x_1 = 0$  and  $x_H = t_1$  (Figure 1). Now for  $t \in (x_h, x_{h+1}]$ , we have  $N_e(t) \approx \exp[\theta_h]$ , where  $\theta_h$  is an unknown model parameter. This implies that  $\boldsymbol{\theta} = \{\theta_h\}_{h=1}^{H-1}$  is a piecewise-constant approximation to  $f(t) = \ln[N_e(t)]$  for  $t \in [s_m, t_1]$ . The piecewise constant population size can be integrated analytically, leading to a discrete approximation to the likelihood in Equation (1). The details of this approximation are provided in Appendix A.

### 2.3 Prior for Effective Population Size Trajectory

Next we develop a prior for the unknown function  $N_e(t)$  that describes the effective population size trajectory over time. Let  $\boldsymbol{\theta} = (\theta_1, \dots, \theta_{H-1})$  be a vector of parameters that govern the effective population size trajectory  $N_e(t)$ . We propose using a SPMRF model (Faulkner and Minin, 2018) for  $\boldsymbol{\theta}$ , which is a type of Markov model where the  $p$ th-order differences in the forward-time evolution of the sequence  $\{\theta_h\}_{h=1}^{H-1}$  are independent and follow a shrinkage prior distribution. The  $p$ th-order forward difference is defined as  $\Delta^p \theta_l \equiv (-1)^p \sum_{j=0}^p (-1)^j \binom{p}{j} \theta_{l+j}$ , for  $l = 1, \dots, H - p - 1$ , and is a discrete approximation to the  $p$ th derivative of  $f(t)$  evaluated at  $t$ . If we assume a horseshoe distribution (Carvalho et al., 2010) as our shrinkage prior on the order- $p$  differences in  $\boldsymbol{\theta}$ , then

$$\Delta \theta_l^p \mid \gamma \sim \mathcal{HS}(\gamma), \quad (2)$$

where  $\gamma$  is the scale parameter of the horseshoe distribution and controls how much we allow  $f(t)$  to vary *a priori*. We put a half-Cauchy prior on  $\gamma$  with scale hyperparameter  $\zeta$ , so that  $\gamma \sim C^+(0, \zeta)$ . Note that the horseshoe distribution is centered at zero. Depending on the order  $p$  of the model, we also place proper priors on  $\theta_1, \dots, \theta_p$ . To do this, we start by setting  $\theta_1 \sim \mathcal{N}(\mu, \sigma^2)$ , where  $\mu$  and  $\sigma$  are hyperparameters typically set to create a diffuse prior. Then for  $p \geq 2$  and  $q = 1, \dots, p - 1$ , we let  $\Delta^q \theta_q \mid \gamma \sim \mathcal{HS}(a_q \gamma)$ , where  $a_q$  depends on  $p$  and  $q$ . For  $p = 2$ , we set  $a_1 = (1/3)^{1/2}$ , and for  $p = 3$ , we set  $a_2 = (3/10)^{1/2}$  and  $a_1 = (1/10)^{1/2}$ . These values are derived from letting the scale of the distribution on  $\Delta \theta_l^p$  be equal to  $\gamma$  and then using the definition of the forward differences to solve for the scale of the lower-order differences. It is rarely of interest to fit a model of order greater than 3, so we do not derive values of  $a_q$  for higher order models here. We will refer to this specific model formulation as a state-space formulation of a horseshoe Markov random field (HSMRF).

The horseshoe distribution is leptokurtic with an infinite spike in density at zero and Cauchy-like tails. In our setting, this combination results in small  $\theta$  differences being shrunk toward zero and larger differences being maintained, which corresponds to smoothing over smaller noisy signals while retaining the ability to adapt to rapid functional changes. This is in contrast to the normal distribution, which has higher density around medium-sized values and normal tails. These attributes result in noisier estimates and reduced ability to capture abrupt functional changes. Different shrinkage priors will result in different levels of shrinkage and therefore different smoothing behavior. Faulkner and Minin (2018) found that the horseshoe prior performed better than the Laplace prior in terms of bias and precision for nonparametric smoothing with SPMRFs, but we do not investigate the effect of different shrinkage priors here.

The horseshoe density does not have a closed form (although see Faulkner and Minin (2018) for an approximation in closed form). However, a horseshoe distribution can be represented hierarchically as a scale mixture of normal distributions by introducing a latent scale parameter that follows a half-Cauchy distribution (Carvalho et al., 2010). That is, if  $\tau_l \sim C^+(0, \gamma)$  and  $\Delta\theta_l^p \mid \tau_l \sim \mathcal{N}(0, \tau_l^2)$ , then integrating over  $\tau_l$  results in the marginal relationship in equation (2).

The hierarchical HSMRF models are a type of  $p$ th-order normal random walk with separate variance parameters for each increment. The inherent Markov properties and properties of the normal distribution allow the joint distribution of  $\theta$  conditional on the vector of scale parameters  $\tau$  to be expressed  $p(\theta \mid \tau, \mu, \sigma^2) = p(\theta_1 \mid \mu, \sigma^2)p(\Delta^p\theta_1, \dots, \Delta^p\theta_{H-p-1} \mid \tau)$ , which results in a multivariate normal distribution with mean  $\mu$  and precision matrix  $\mathbf{Q}(\tau)$ . Specifically,  $\theta$  follows a Gaussian Markov random field (GMRF; Rue and Held, 2005) conditional on  $\tau$ , where the order  $p$  of the differencing in  $\theta$  determines the structure of the sparse  $\mathbf{Q}(\tau)$ . For the models presented here,  $\mu = \mu\mathbf{1}$ , where  $\mu$  is a constant and  $\mathbf{1}$  is a vector of ones. We specify  $p(\tau)$  by assuming that the  $\tau$ 's are independent  $C^+(0, \gamma)$ -distributed random variables, where  $\tau_l \sim C^+(0, \gamma)$  for  $l = p, \dots, H - p - 1$  and  $\tau_l \sim C^+(0, a_l\gamma)$  for  $l = 1, \dots, p - 1$ . The marginal joint distribution of  $\theta$  that results from integrating over  $\tau$  is a HSMRF. Note that a GMRF model results when a single scale parameter  $\tau$  is used for all order- $p$  differences in  $\theta$ . For our GMRF models, we use  $\tau \sim C^+(0, \zeta)$ , where  $\zeta$  is a fixed hyperparameter. The order of the HSMRF will determine the amount of smoothing, with higher orders resulting in more smoothing. We only consider first-order and second-order models here. In practice, we use the state-space formulation described previously but with the independent hierarchical representations of the horseshoe distributions for the individual order- $p$  differences, which improves computational efficiency over the conditional multivariate normal representation.

## 2.4 Posterior Inference

For the case where we have a fixed genealogical tree,  $\mathbf{g}$ , which consists of sampling times  $s$  and coalescent times  $t$ , the posterior distribution of the parameters  $\{\theta, \tau, \gamma\}$  can be written as

$$p(\theta, \tau, \gamma \mid \mathbf{g}) \propto p(\mathbf{g} \mid \theta)p(\theta \mid \tau)p(\tau \mid \gamma)p(\gamma). \quad (3)$$

Here  $\mathbf{g}$  is considered data and we assume the coalescent times are known. Then  $p(\mathbf{g} \mid \theta)$  is the coalescent likelihood and  $p(\theta \mid \tau)p(\tau \mid \gamma)p(\gamma)$  is the HSMRF prior described in Section 2.3. For our GMRF models, the righthand side of equation 3 becomes  $p(\mathbf{g} \mid \theta)p(\theta \mid \tau)p(\tau)$ .

For our analyses with fixed genealogical trees, we follow Faulkner and Minin (2018) and Lan et al. (2015) and use Hamiltonian Monte Carlo (HMC; Neal, 2011) for posterior inference. HMC performs joint proposals for the parameters that are typically far from the current parameter state and have high acceptance rates, resulting in efficient posterior sampling. We used the Stan computing environment (Carpenter et al., 2016) for implementing HMC. Specifically,

we used the open source package `rstan` (Stan Development Team, 2017), which provides a platform for fitting models using HMC in the R computing environment (R Core Team, 2017). Our R package titled `spmrf` allows for easy implementation of our models for use on fixed genealogical trees via a wrapper to the `rstan` tools. The package code is publicly available at <https://github.com/jrfaulkner/spmrf>. We present a method for objectively setting the scale hyperparameter  $\zeta$  of the prior distribution of the global smoothing parameter  $\gamma$  in Appendix B.

When there are genetic sequence data available and we want to jointly estimate evolutionary parameters, coalescent times, and population size trajectories, our posterior can be written as

$$p(\mathbf{g}, \mathbf{\Omega}, \boldsymbol{\theta}, \boldsymbol{\tau}, \gamma \mid \mathbf{Y}) \propto p(\mathbf{Y} \mid \mathbf{g}, \mathbf{\Omega})p(\mathbf{g} \mid \boldsymbol{\theta})p(\mathbf{\Omega})p(\boldsymbol{\theta} \mid \boldsymbol{\tau})p(\boldsymbol{\tau} \mid \gamma)p(\gamma), \quad (4)$$

where  $\mathbf{Y}$  are the sequence data and  $\mathbf{\Omega}$  are the parameters related to the DNA substitution model. The likelihood of the sequence data given the parameters is  $p(\mathbf{Y} \mid \mathbf{g}, \mathbf{\Omega})$ , and now  $p(\mathbf{g} \mid \boldsymbol{\theta})$  is a prior for the coalescent times. The remaining components are the prior for the evolution parameters  $p(\mathbf{\Omega})$  and the HSMRF prior as in equation (3). HMC requires the calculation of gradients over continuous parameter space and therefore cannot be used for inference on discrete parameters. To the best of our knowledge, HMC has not been fully developed for inference on phylogenetic trees due to the presence of discrete parameters related to the tree configuration, although some recent progress has been made by Dinh et al. (2017). Therefore, we developed a custom MCMC algorithm that uses a combination of Gibbs sampling, elliptical slice sampling, and the Metropolis-Hastings (MH) algorithm to sample from the joint posterior of the evolution parameters and the effective population size parameters. In particular, elliptical slice sampling (Murray et al., 2010) was used to sample from the joint field of log effective population sizes conditional on the latent scale parameters, a Gibbs sampler based on an approach developed by (Makalic and Schmidt, 2016) for horseshoe random variables was used to sample the latent scale parameters conditional on the field parameters, and standard phylogenetic MH steps were used to update the genealogy and substitution model parameters. We implemented our custom MCMC in `RevBayes` — a statistical computing environment geared primarily for phylogenetic inference (Höhna et al., 2016). The standard phylogenetic MH updates mentioned above were already implemented in `RevBayes`, so we contributed a heterochronous coalescent likelihood calculator, elliptical slice sampling, and Gibbs updates of our model parameters to the `RevBayes` source code. The details of the sampling scheme are provided in the Appendix C and code for implementing our methods for analyzing sequence data is available at <https://github.com/jrfaulkner/phylocode>.

## 3 Results

### 3.1 Simulated Data

We used simulated data to assess the performance of the HSMRF model relative to the GMRF model. We investigated four scenarios with different trajectories for  $N_e(t)$ : (1) Bottleneck (BN), (2) Boom-Bust (BB), (3) Broken Exponential (BE), and (4) Nonstationary Gaussian Process (NGP) realization. The trajectory shapes are shown at the top of Figure 2. For each scenario, we generated 100 data sets of coalescent times and fit GMRF and HSMRF models of first and second order using the fixed-tree approach. The scenario descriptions and further methodological details of the simulations are provided in Appendix D.

We assessed the relative performance of the models using a set of summary statistics. As a measure of bias, we used the mean absolute deviation (MAD) to compare the posterior me-

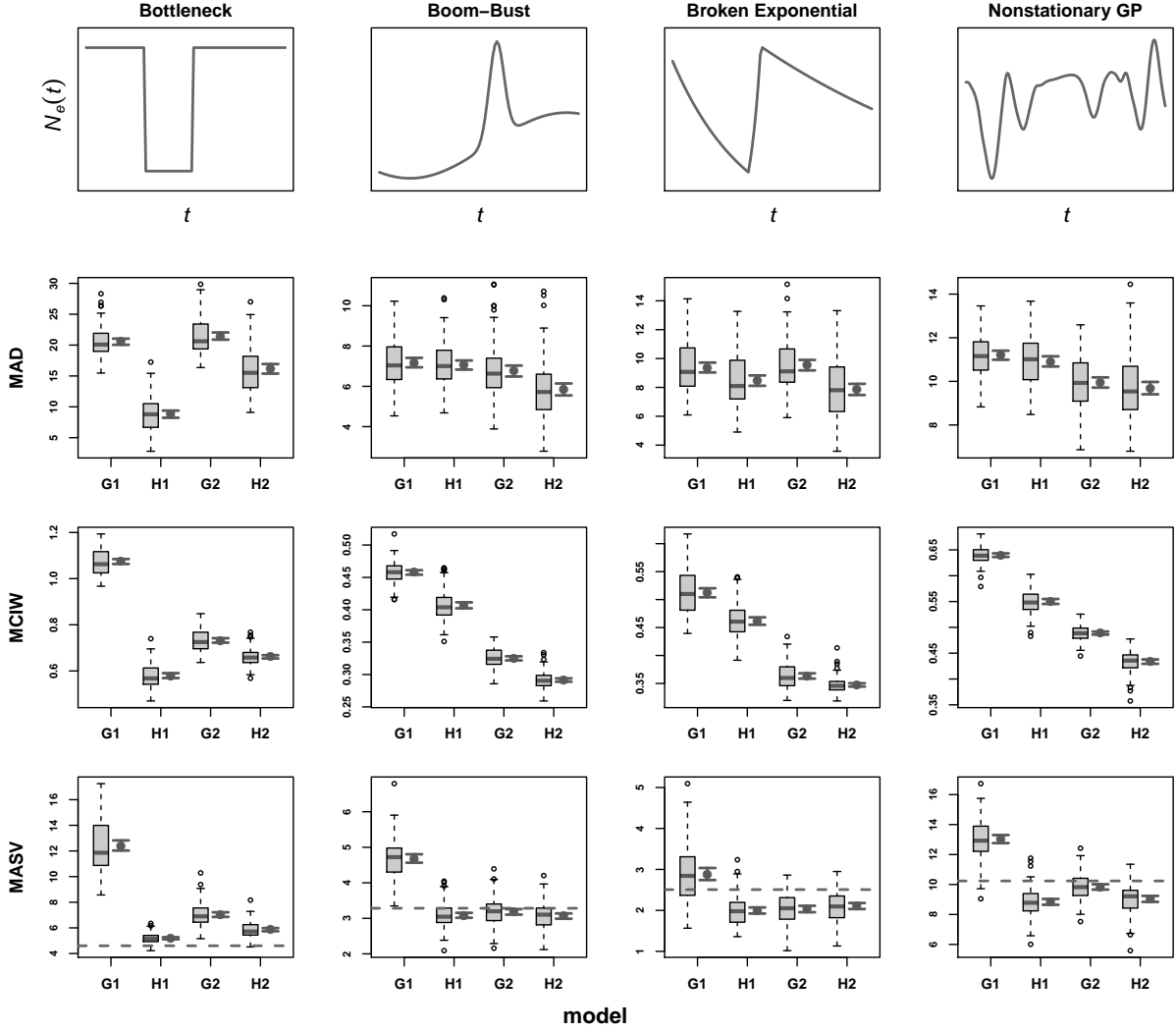


Figure 2: Effective population size trajectories used in simulations and simulation results by model and scenario. Models are GMRF of order 1 (G1) and order 2 (G2) and HSMRF of order 1 (H1) and order 2 (H2). Top row shows true effective population size trajectories used to simulate coalescent data. Remaining rows show mean absolute deviation (MAD), mean credible interval width (MCIW), and mean absolute sequential variation (MASV). Horizontal dashed line in plots on bottom row is the true mean absolute sequential variation (TMASV). Shown for each model are standard boxplots of simulation results (left) and mean values with 95% frequentist confidence intervals (right).

dians of the trend parameters ( $\hat{\theta}_i$ ) to the true trend values ( $\theta_i$ ):  $MAD = \frac{1}{H-1} \sum_{i=1}^{H-1} |\hat{\theta}_i - \theta_i|$ . We assessed the width of the 95% Bayesian credible intervals (BCIs) using the mean credible interval width (MCIW):  $MCIW = \frac{1}{H-1} \sum_{i=1}^{H-1} (\hat{\theta}_{97.5,i} - \hat{\theta}_{2.5,i})$ , where  $\hat{\theta}_{97.5,i}$  and  $\hat{\theta}_{2.5,i}$  are the 97.5% and 2.5% quantiles of the posterior distribution for  $\theta_i$ . To measure local variability in the estimated population trend, we used the mean absolute sequential variation (MASV) of  $\hat{\theta}$ , which was computed as  $MASV = \frac{1}{H-2} \sum_{i=1}^{H-2} |\hat{\theta}_{i+1} - \hat{\theta}_i|$ . We compared the observed MASV to the true MASV (TMASV) in the underlying trend function, which is calculated by substituting true  $\theta$ 's into the equation for MASV. For a measure of model complexity, we estimated the effective number of parameters  $p_{eff}$  using an approach suggested by Raftery et al. (2006):



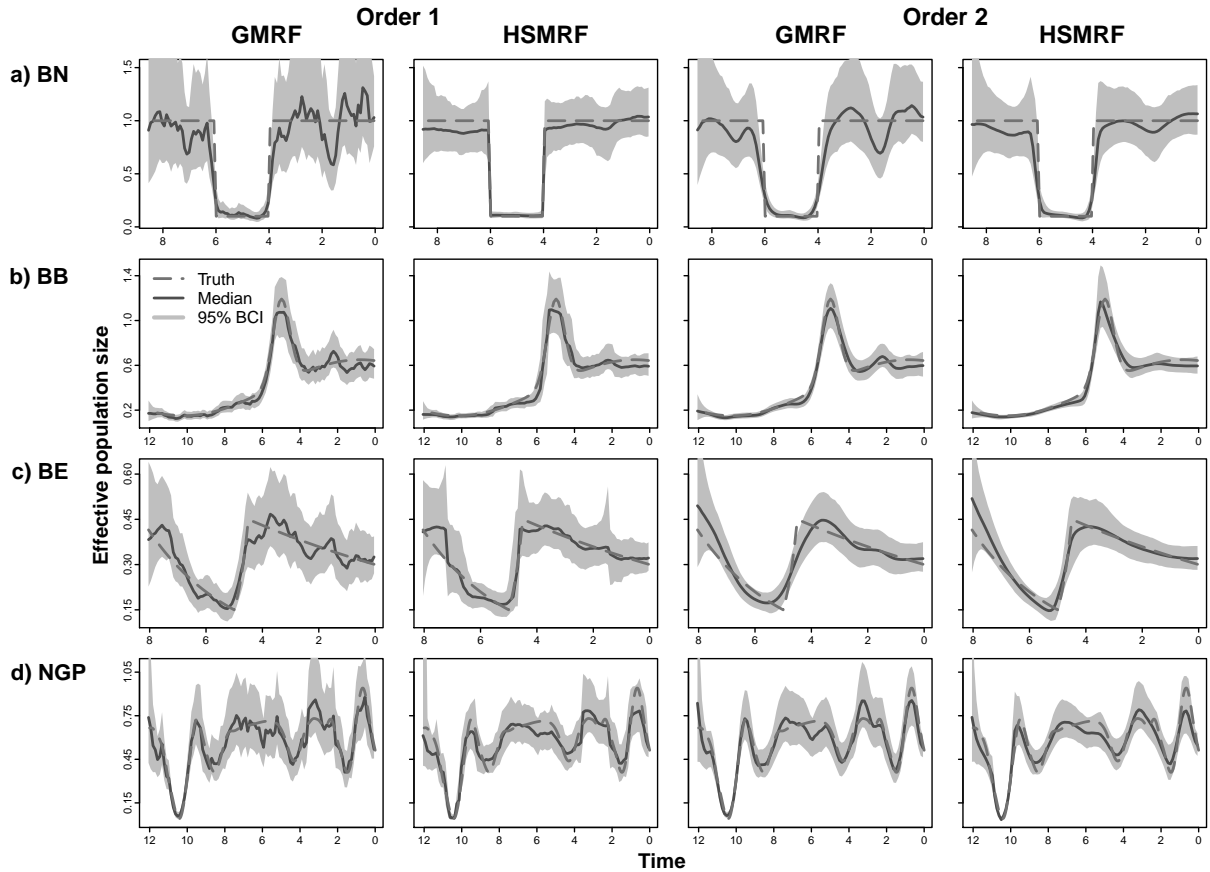


Figure 3: Example fits of first- and second-order Gaussian Markov random field (GMRF) and horseshoe Markov random field (HSMRF) models for four different simulation scenarios. Scenarios are a) Bottleneck (BN), b) Boom-Bust (BB), c) Broken Exponential (BE), and d) Non-stationary Gaussian Process (NGP). Results for all models within a particular scenario are for the same set of simulated data. Shown are the true effective population size trajectories that generated the data (dashed line), posterior medians of estimated trajectories (solid line) and associated 95% Bayesian credible intervals (shaded band).

$p_{eff} = \frac{2}{R-1} \sum_{r=1}^R (\mathcal{L}_r - \bar{\mathcal{L}})^2$ , where  $\mathcal{L}_r$  is the log-likelihood evaluated at the parameter values for the  $r$ th of  $R$  samples from the posterior, and  $\bar{\mathcal{L}}$  is the mean value of  $\mathcal{L}$  across the  $R$  samples. For a measure of computational efficiency, we calculated the mean effective sample size (ESS) of the posterior samples across parameters for each model and simulated data set and used those with the total sampling times to calculate the mean ESS per second of sampling time.

For the BN scenario, the HSMRF model clearly had better performance than the GMRF model for the main performance metrics for both model orders (Figure 2, Table 1). Example model fits from each scenario provide some intuition for the simulation results (Figure 3). First order models did better than second order models within model types for the BN scenario. Differences between model types were not as strong for the other scenarios. The second-order HSMRF performed the best in terms of MAD and MCIW for the remaining scenarios. However, the HSMRF models were not noticeably different from the second-order GMRF in terms of MASV for the BB and BE scenarios. The second-order GMRF had mean MASV closer to TMAV than did the second-order HSMRF for the NGP scenario. Although the GMRF tended to estimate excess variation in the middle section of the trend for the NGP

Table 1: Mean values of performance measures across 100 simulations for each model and scenario. Models are GMRF of order 1 (G1) and order 2 (G2) and HSMRF of order 1 (H1) and order 2 (H2). Abbreviations are mean absolute deviation (MAD), mean credible interval width (MCIW), mean absolute sequential variation (MASV), true MASV (TMASV), effective number of parameters ( $p_{eff}$ ), and effective sample size (ESS). Values of MAD, MRW, MCIW, MASV, and TMASV are multiplied by 100 for readability.

Scenario	Model	MAD	MCIW	MASV	TMASV	$p_{eff}$	ESS/s
Bottleneck	G1	20.55	1.07	12.43	4.61	30.5	8.78
	H1	8.81	0.58	5.19	4.61	10.5	3.01
	G2	21.47	0.73	7.04	4.61	15.8	0.89
	H2	16.16	0.66	5.86	4.61	14.3	0.26
Boom-Bust	G1	7.18	0.46	4.68	3.28	25.6	9.25
	H1	7.06	0.41	3.08	3.28	21.6	1.53
	G2	6.76	0.32	3.18	3.28	13.1	0.80
	H2	5.85	0.29	3.06	3.28	10.9	0.20
Broken Exp.	G1	9.38	0.51	2.89	2.51	15.5	8.42
	H1	8.47	0.46	2.00	2.51	13.5	2.29
	G2	9.54	0.36	2.03	2.51	8.2	1.57
	H2	7.86	0.35	2.11	2.51	7.7	0.56
Nonstationary GP	G1	11.20	0.64	13.03	10.24	46.1	1.91
	H1	10.92	0.55	8.84	10.24	37.3	0.56
	G2	9.95	0.49	9.84	10.24	28.1	0.08
	H2	9.69	0.43	9.04	10.24	23.5	0.05

scenario, it did capture the peaks and troughs a little better than the HSMRF in other parts of the trend (see Figure 3 for an example). In all scenarios, the HSMRF had lower  $p_{eff}$  compared to the GMRF of the same order. The GMRF was consistently more computationally efficient than the HSMRF, with mean ESS/sec approximately 1.5 to 6 times higher for models of the same order. These differences are due to the additional parameters in the HSMRF models. The second-order models were relatively slow for both model types, but the HSMRF was always slower.

### 3.2 Egyptian Hepatitis C Virus

The hepatitis C virus (HCV) is a blood-borne RNA virus that exclusively infects humans. HCV infection is often asymptomatic, but can lead to liver disease and liver failure. HCV infections have historically had high prevalence in Egypt (Miller and Abu-Raddad, 2010). This is thought to be due to past widespread use of unsanitary medical practices in the region. A particular example of interest is a treatment for the parasite disease schistosomiasis known as parenteral antischistosomal therapy (PAT), which uses intravenous injections. PAT was practiced from the 1920's to 1980's in Egypt and is thought to have contributed to the spread of HCV during that period due to unsterilized injection equipment (Frank et al., 2000; Medhat et al., 2002).

We analyze 63 RNA sequences of type 4 with 411 base pairs from the E1 region of the HCV genome that were collected in 1993 in Egypt (Ray et al., 2000). Pybus et al. (2003) used a piecewise demographic model for effective population size with a period of exponential

growth between two periods of constant population size and concluded that the HCV population grew exponentially during the period of PAT treatment. Other authors have applied nonparametric methods to estimate the effective population size trajectory for these data (*e.g.*, Drummond et al., 2005; Minin et al., 2008; Palacios and Minin, 2013). Different nonparametric methods lead to different estimated trajectories and different levels of uncertainty. This example is interesting for both the nature of the change in population size and for the period before 1900 with few coalescent times.

We fit four different models to these data: 1) Bayesian Skyline — a piecewise constant/linear model with estimable locations of change-points (BSKL; Drummond et al., 2005), 2) Bayesian Skyride (BSKR; Minin et al., 2008) 3) GMRF (equivalent to Bayesian Skygrid, Gill et al. (2013)), and 4) our HSMRF model. We note that the BSKR model is also a type of GMRF model where the non-uniform grid cell boundaries are determined by coalescent events. For all four models we jointly estimated the evolution parameters, the genealogies, and the effective population size parameters. We used the program BEAST implementation of the BSKL and BSKR models (Drummond et al., 2012), and used our own RevBayes implementation of the GMRF and HSMRF models. Although the GMRF model is available in BEAST, the HSMRF is not, so we decided to use common software for the GMRF and HSMRF models. We used the same distributional forms and parameterizations for priors representing model components in common across the models. Where possible, we also attempted to use the same proposal distributions and maintain the same relative weighting of different MCMC moves in common to the models across the two software packages. We fixed the mean mutation rate to  $7.9 \times 10^{-4}$  substitutions/site/year, which is a value estimated by Pybus et al. (2001) and used by others for these data. We used the HKY nucleotide substitution model (Hasegawa et al., 1985) with gamma distributed rate heterogeneity and invariant sites (Yang, 1994). For the GMRF and HSMRF models we used 101 equally-spaced grid cells where the first 100 ended at a fixed boundary of 278 years before 1993, and the final cell captured any coalescent events beyond the boundary. The BSKL model requires specification of the number of discrete population intervals, where each interval describes a piecewise constant population size between two coalescent events. We used 40 population groups to allow fair flexibility to capture sharp features in the population trend. The BSKR model uses first-order differencing, so we also used first-order formulations for the GMRF and HSMRF models.

The four methods differed in both the estimated trajectories and the uncertainty about those trajectories (Figure 4). The shape of the median trajectory from the HSMRF model was most similar to that of the BSKL model, yet the HSMRF model showed a very rapid increase in population between 1925 and 1945, while the BSKL and other models showed more gradual increases that started earlier and ended later. The increase estimated by the BSKR model lasted the longest, starting near 1900 and ending near 1970. The HSMRF and the BSKL also showed relatively constant population size following the increase in the mid 20th century, while the BSKR and GMRF models showed a decrease after 1970. The HSMRF model had the most uncertainty in the time period prior to the year 1900, but the marginal posteriors in that region were actually highly skewed with long tails in the direction of higher population sizes and with 90% of the posterior density below population sizes of approximately  $10^5$  (not shown). This high uncertainty was due the lack of coalescent times during that period. The GMRF model also displayed high uncertainty in this region relative to the other two models, but it probably did not display as much uncertainty as the HSMRF because it is not flexible enough to fit the increase after 1920 and still allow a high population size prior to 1900 in the way that the HSMRF model did. Both the BSKL and BSKR models had narrow credible intervals in the period prior to 1900, with the BSKR model showing more uncertainty than the BSKL. Both of

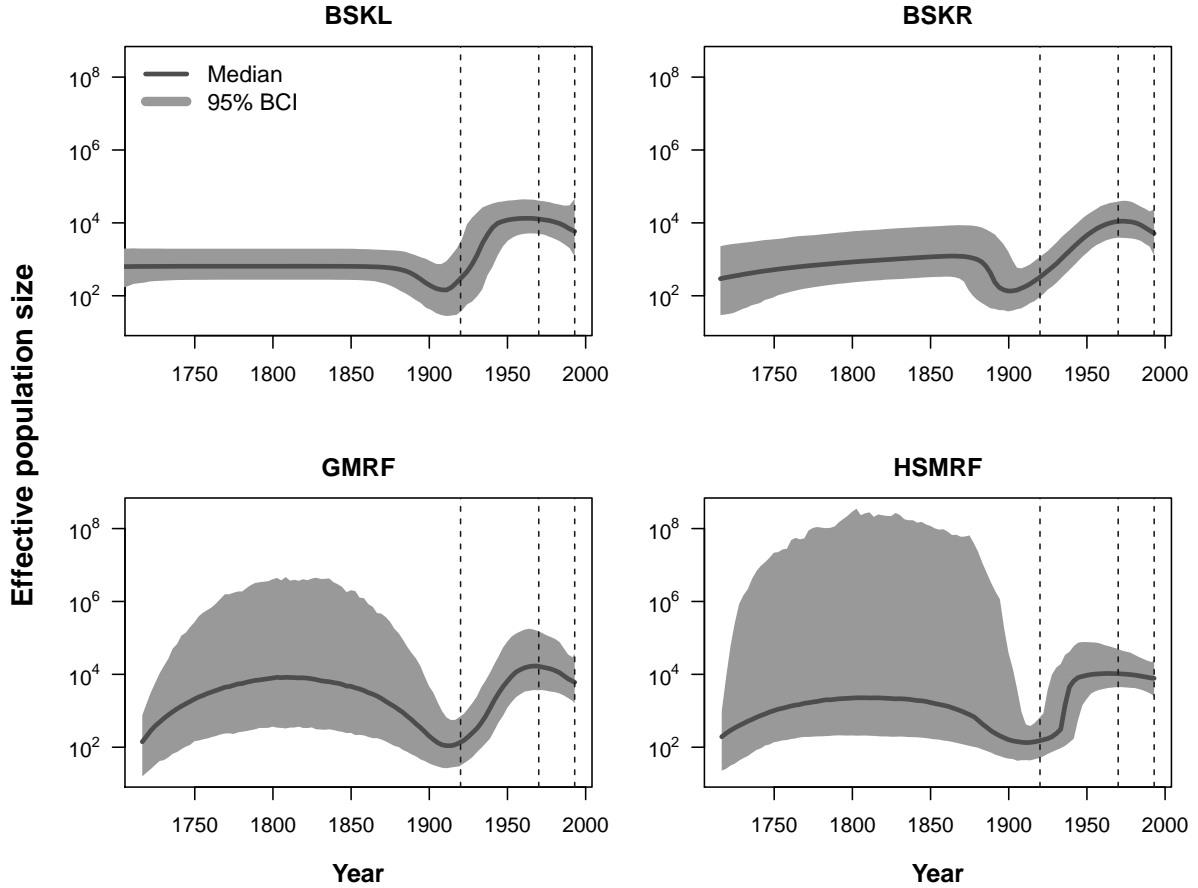


Figure 4: Posterior medians (solid black lines) of effective population sizes and associated 95% credible intervals (grey shaded areas) for the HCV data for the Bayesian Skyline (BSKL), Bayesian Skyride (BSKR), Gaussian Markov random field (GMRF), and horseshoe Markov random field (HSMRF) models. Vertical reference lines are shown at years 1920, 1970, and 1993.

these models use piecewise constant trajectories between coalescent events, which means they are restricted to be nearly flat over the long period without coalescent events. The uncertainty in that region was therefore grossly underestimated due to the constrained nature of those models.

### 3.3 Beringian Steppe Bison

Modern molecular methods have allowed the recovery of DNA samples from specimens that lived hundreds to hundreds of thousands of years ago (Pääbo et al., 2004; Shapiro and Hofreiter, 2014). Large mammals that lived in the Northern Hemisphere during the Pleistocene and Holocene epochs have been a valuable source of this ancient DNA due to conditions favorable for specimen preservation in the northern latitudes (*e.g.*, Shapiro et al., 2004; Lorenzen et al., 2011). We focus on bison (*Bison* spp.) that lived on the steppe-tundra of Northern Asia and Europe and crossed into North America over the Bering land bridge during the middle Pleistocene (Shapiro et al., 2004). Interest has been in determining whether human impact or climate and related habitat change were behind the decline of bison across their range during the late Pleistocene. Shapiro et al. (2004) used a parametric piecewise-exponential model for the bison effective population size and estimated that the time of transition from population growth

to decline was 37 thousand years ago (kya). Drummond et al. (2005) used the more flexible BSKL model, which indicated a more rounded and prolonged peak in population size followed by a rapid decline and bottleneck around 10 kya. Here we use a modified version of the bison data described by Shapiro et al. (2004) and fit coalescent models directly to the sequence data as with the HCV data. We make qualitative comparisons among the resulting estimated population trajectories and in relation to some benchmark times describing the arrival of humans and the period of the Last Glacial Maximum (LGM). In Appendix E we perform additional analyses that apply GMRF and HSMRF models of first and second order to a fixed genealogy derived from the sequence data and we use Bayes factors to compare the model performance.

We analyze 152 sequences (135 ancient and 17 modern) of mitochondrial DNA with 602 base pairs from the mitochondrial control region. DNA was extracted from bison fossils from Alaska (68), Canada (46), Siberia (13), the lower 48 United States (6), and China (2). Sample dates were estimated for the ancient samples using radiocarbon dating, with dates ranging up to 59k years. We treat the calibrated radiocarbon dates as known in the following analyses. These data are the same as those used by Gill et al. (2013), and are slightly modified from the data first described by Shapiro et al. (2004) to remove sequences identified as potentially contaminated with young radiocarbon (Shapiro et al., 2010) and include additional sequences generated since generation of the initial data set. In this data set, radiocarbon dates are calibrated to calendar time using the IntCal09 calibration curve (Reimer et al., 2009).

The LGM in the Northern Hemisphere is estimated to have occurred between 26.5 to 19 kya (Clark et al., 2009). A small, isolated population of humans existed in central Beringia, including, potentially, the land bridge that connected the continents during the LGM (Llamas et al., 2016). Humans may have ventured into eastern Beringia (Alaska and Yukon) as early as 26 kya (Bourgeon et al., 2017), but there is as yet no evidence of continuous occupation until 14 kya (Easton et al., 2011; Holmes, 2011). Humans probably first entered continental North America via a western coastal route that became available close to 16 kya (Llamas et al., 2016; Heintzman et al., 2016), where they would have encountered the population of steppe bison that were isolated in the south with the coalescence of the Laurentide and Cordilleran glaciers (Shapiro et al., 2004; Heintzman et al., 2016). Because the majority of our bison samples were collected in North America, we used 16-14 kya as the time of first human occupation.

As with the HCV data, we used BEAST to fit the BSKL and BSKR models and used RevBayes to fit the GMRF and HSMRF models. We used 15 groups for the BSKL model to match the approach used by Drummond et al. (2005), which allowed for sufficient flexibility to fit important change points without introducing computational challenges associated with more groups. To improve mixing and reduce computation time, we used a strict molecular clock with mutation rate set to  $5.38 \times 10^{-7}$  substitutions per year, which was based on initial runs in BEAST where the clock rate was estimated under a GMRF model for the effective population sizes. We used the HKY nucleotide substitution model with gamma distributed rate heterogeneity.

Results indicated quite different population trajectories from the different models (Figure 5). The posterior median trajectory from the HSMRF model was most similar to the BSKL model, but the credible intervals for the HSMRF model were most similar to the GMRF model. The BSKL model underestimated the uncertainty in the population trajectory over areas assumed to have constant population size. The BSKR and GMRF models did not have the flexibility to capture rapid changes in trend that the HSMRF, and to a lesser extent, BSKL models did. The HSMRF model displayed a more complex descent from the peak size to the present in comparison to the other models, and the areas of rapid descent are coincident with the arrival of humans in eastern Beringia and ice-free North America and the initial retreat of the glaciers,

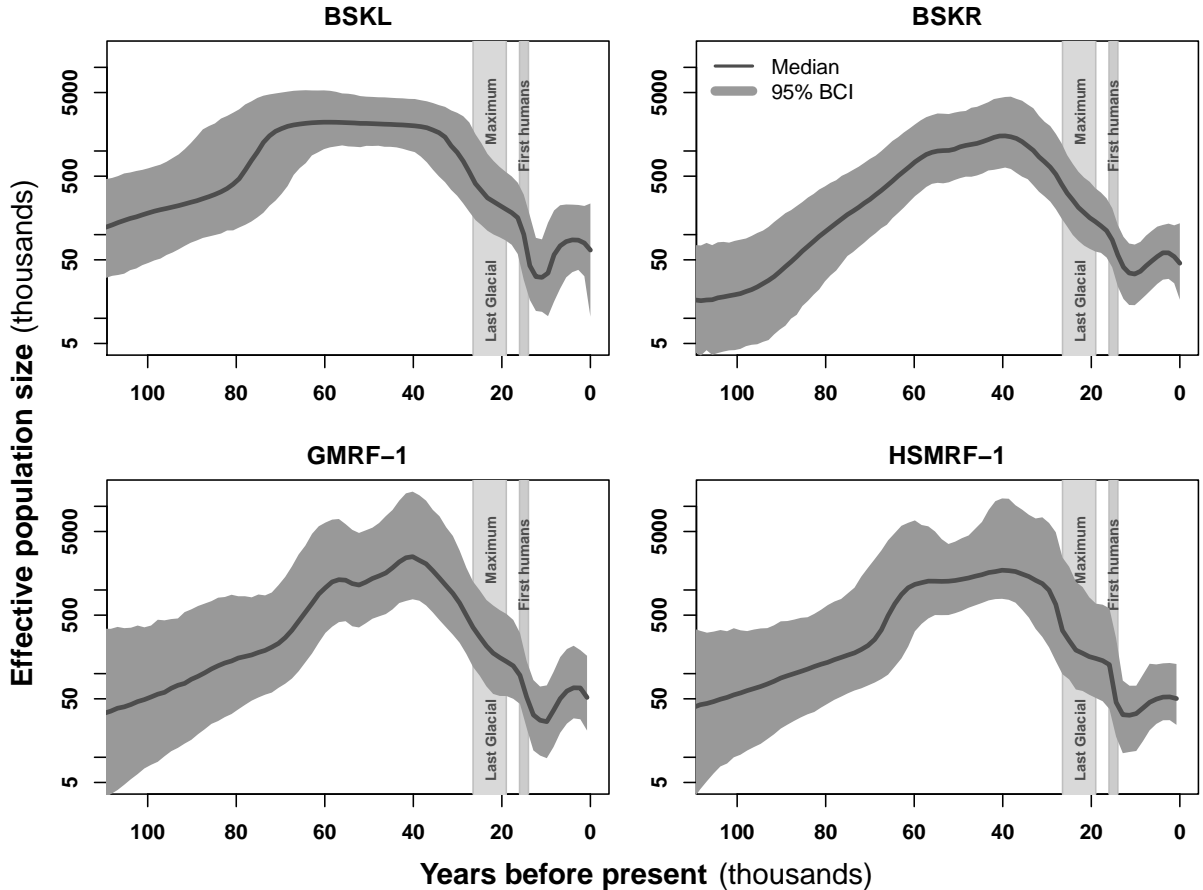


Figure 5: Posterior medians of effective population sizes and associated 95% credible intervals obtained from the bison DNA sequence data using the Bayesian SkyLine (BSKY) with 15 groups, Bayesian SkyRide (BSKR), and order-1 GMRF and HSMRF models. The effective population sizes and evolution process are estimated jointly for each of these models. The period of the Last Glacial Maximum and timing of first human settlement in North America are shown for reference.

both of which are coincident with changes in habitat.

## 4 Discussion

We introduced a novel and fully Bayesian method for nonparametric inference for phylodynamics that we call the HSMRF. This method utilizes a shrinkage prior known as the horseshoe distribution, which allows more flexibility in the possible forms of the effective population size trajectories, yet also generates smoother trajectories in comparison to standard GMRF methods. Our simulations demonstrated that the HSMRF had lower bias and higher precision than the GMRF and was able to recover the underlying true trajectories better in most cases. We introduced a new joint model for the coalescent and HSMRF prior, and we presented a new MCMC scheme using Gibbs sampling in combination with elliptical slice sampling that resulted in efficient, high-dimensional block updates for the effective population size parameters and latent scale parameters without tuning parameters.

Our HCV example showed that the HSMRF can have more uncertainty than the GMRF in

certain cases where data are sparse. However, the HSMRF also showed that HCV may have undergone a sharper increase in effective population size than previous estimates had shown. In addition, the HSMRF-estimated timing of this increase was later than other method's estimates. The later increase is more plausible in light of other epidemiological information that links increased prevalence of HCV in Egypt with mass administration of parenteral antischistosomal therapy (Frank et al., 2000; Medhat et al., 2002). Although it was not conclusive which model was the best in the bison example, the first-order HSMRF model captured some features in the population trajectory that the corresponding GMRF did not. Our results from both data examples indicated that the properties of the population size trajectories estimated by the HSMRF model were somewhere between those from the GMRF model and the BSKL model. The BSKL model is a type of change-point model, which suggests the HSMRF can produce behavior of change-point models without explicitly needing to specify number or location of change points.

It is possible that shrinkage priors other than the horseshoe could provide better performance for nonparametric phylodynamic inference. The Cauchy-like tails of the horseshoe distribution can create challenges for MCMC due to the complexities of the posterior parameter space. One could use a half- $t$ -distribution with low degrees of freedom (2 to 5) in place of the half-Cauchy on the individual scale parameters ( $\tau$ ). We have informally investigated these shrinkage priors based on half- $t$ -distributions and found they resulted in similar smoothing as the horseshoe but their ability to capture abrupt functional changes diminishes with increasing degrees of freedom. Other shrinkage priors such as the double-Weibull (Reményi and Vidakovic, 2015) and Dirichlet-Laplace (Bhattacharya et al., 2015) could be promising options due to their favorable shrinkage properties. We have not investigated other shrinkage priors for nonparametric smoothing in phylodynamics, but further research in that direction could be productive.

## Acknowledgments

J.R.F. and V.N.M. were supported by the NIH grant U54 GM111274. V.N.M. was supported by the NIH grant R01 AI107034. A.F.M. was supported by ARCS Foundation Fellowship.

## Supplementary Materials

The code for implementing our methods for estimation of population size changes directly from molecular sequence data is available at <https://github.com/jrfaulkner/phylocode>.

## References

- Alizon, S., Lion, S., Murall, C. L., and Abbate, J. L. (2014). Quantifying the epidemic spread of Ebola virus (EBOV) in Sierra Leone using phylodynamics. *Virulence* **5**, 825–827.
- Anderson, P. M. and Lozhkin, A. V. (2001). The Stage 3 interstadial complex (Karginskii/middle Wisconsinan interval) of Beringia: variations in paleoenvironments and implications for paleoclimatic interpretations. *Quaternary Science Reviews* **20**, 93–125.
- Bhattacharya, A., Pati, D., Pillai, N. S., and Dunson, D. B. (2015). Dirichlet-Laplace priors for optimal shrinkage. *Journal of the American Statistical Association* **110**, 1479–1490.

- Bourgeon, L., Burke, A., and Higham, T. (2017). Earliest human presence in North America dated to the last glacial maximum: new radiocarbon dates from Bluefish Caves, Canada. *PloS ONE* **12**, e0169486.
- Carpenter, B., Gelman, A., Hoffman, M., Lee, D., Goodrich, B., Betancourt, M., Brubaker, M. A., Guo, J., Li, P., and Riddell, A. (2016). Stan: A probabilistic programming language. *Journal of Statistical Software* **20**, 1–37.
- Carvalho, C. M., Polson, N. G., and Scott, J. G. (2010). The horseshoe estimator for sparse signals. *Biometrika* **97**, 465–480.
- Clark, P. U., Dyke, A. S., Shakun, J. D., Carlson, A. E., Clark, J., Wohlfarth, B., Mitrovica, J. X., Hostetler, S. W., and McCabe, A. M. (2009). The last glacial maximum. *Science* **325**, 710–714.
- Dinh, V., Bilge, A., Zhang, C., and Matsen, IV, F. A. (2017). Probabilistic path Hamiltonian Monte Carlo. In *Proceedings of the 34th International Conference on Machine Learning*, volume 70, pages 1009–1018.
- Drummond, A. J., Rambaut, A., Shapiro, B., and Pybus, O. G. (2005). Bayesian coalescent inference of past population dynamics from molecular sequences. *Molecular Biology and Evolution* **22**, 1185–1192.
- Drummond, A. J., Suchard, M. A., Xie, D., and Rambaut, A. (2012). Bayesian phylogenetics with BEAUti and the BEAST 1.7. *Molecular Biology and Evolution* **29**, 1969–1973.
- Easton, N. A., Mackay, G. R., Young, P. B., Schnurr, P., and Yesner, D. R. (2011). Chindadn in Canada? emergent evidence of the Pleistocene transition in southeast Beringia as revealed by the Little John Site, Yukon. In *From the Yenisei to the Yukon: Interpreting Lithic Assemblage Variability in Late Pleistocene/Early Holocene Beringia*, pages 289–307. Texas A&M University Press.
- Faulkner, J. R. and Minin, V. N. (2018). Locally adaptive smoothing with Markov random fields and shrinkage priors. *Bayesian Analysis* **13**, 225–252.
- Felsenstein, J. (1981). Evolutionary trees from DNA sequences: a maximum likelihood approach. *Journal of Molecular Evolution* **17**, 368–376.
- Felsenstein, J. and Rodrigo, A. G. (1999). Coalescent approaches to HIV population genetics. In Crandall, K. A., editor, *The Evolution of HIV*, pages 233–272. Johns Hopkins University Press.
- Frank, C., Mohamed, M. K., Strickland, G. T., Lavanchy, D., Arthur, R. R., Magder, L. S., El Khoby, T., Abdel-Wahab, Y., Anwar, W., and Sallam, I. (2000). The role of parenteral antischistosomal therapy in the spread of hepatitis C virus in Egypt. *The Lancet* **355**, 887–891.
- Fuentes, M. (2002). Spectral methods for nonstationary spatial processes. *Biometrika* **89**, 197–210.
- Gill, M. S., Lemey, P., Faria, N. R., Rambaut, A., Shapiro, B., and Suchard, M. A. (2013). Improving Bayesian population dynamics inference: a coalescent-based model for multiple loci. *Molecular Biology and Evolution* **30**, 713–724.



- Griffiths, R. C. and Tavaré, S. (1994). Sampling theory for neutral alleles in a varying environment. *Philosophical Transactions of the Royal Society of London B: Biological Sciences* **344**, 403–410.
- Gronau, Q. F., Singmann, H., and Wagenmakers, E.-J. (2017). bridgesampling: An R package for estimating normalizing constants. *arXiv preprint arXiv:1710.08162* .
- Hasegawa, M., Kishino, H., and Yano, T. (1985). Dating of the human-ape splitting by a molecular clock of mitochondrial DNA. *Journal of Molecular Evolution* **22**, 160–174.
- Heintzman, P. D., Froese, D., Ives, J. W., Soares, A. E., Zazula, G. D., Letts, B., Andrews, T. D., Driver, J. C., Hall, E., Hare, P. G., et al. (2016). Bison phylogeography constrains dispersal and viability of the Ice Free Corridor in western Canada. *Proceedings of the National Academy of Sciences* **113**, 8057–8063.
- Higdon, D. (1998). A process-convolution approach to modelling temperatures in the North Atlantic Ocean. *Environmental and Ecological Statistics* **5**, 173–190.
- Höhna, S., Landis, M. J., Heath, T. A., Boussau, B., Lartillot, N., Moore, B. R., Huelsenbeck, J. P., and Ronquist, F. (2016). RevBayes: Bayesian phylogenetic inference using graphical models and an interactive model-specification language. *Systematic Biology* **65**, 726–736.
- Holmes, C. E. (2011). The Beringian and Transitional periods in Alaska. In *From the Yenisei to the Yukon: Interpreting Lithic Assemblage Variability in Late Pleistocene/Early Holocene Beringia*, pages 179–191. Texas A&M University Press.
- Kass, R. E. and Raftery, A. E. (1995). Bayes factors. *Journal of the American Statistical Association* **90**, 773–795.
- Kingman, J. F. C. (1982). The coalescent. *Stochastic Processes and Their Applications* **13**, 235–248.
- Lan, S., Palacios, J. A., Karcher, M., Minin, V. N., and Shahbaba, B. (2015). An efficient Bayesian inference framework for coalescent-based nonparametric phylodynamics. *Bioinformatics* **31**, 3282–3289.
- Llamas, B., Fehren-Schmitz, L., Valverde, G., Soubrier, J., Mallick, S., Rohland, N., Nordenfelt, S., Valdiosera, C., Richards, S. M., Rohrlach, A., et al. (2016). Ancient mitochondrial DNA provides high-resolution time scale of the peopling of the Americas. *Science Advances* **2**, e1501385.
- Lorenzen, E. D., Nogués-Bravo, D., Orlando, L., Weinstock, J., Binladen, J., Marske, K. A., Ugan, A., Borregaard, M. K., Gilbert, M. T. P., Nielsen, R., et al. (2011). Species-specific responses of Late Quaternary megafauna to climate and humans. *Nature* **479**, 359–364.
- Makalic, E. and Schmidt, D. F. (2016). A simple sampler for the horseshoe estimator. *IEEE Signal Processing Letters* **23**, 179–182.
- Medhat, A., Shehata, M., Magder, L. S., Mikhail, N., Abdel-Baki, L., Nafeh, M., Abdel-Hamid, M., Strickland, G. T., and Fix, A. D. (2002). Hepatitis C in a community in upper Egypt: risk factors for infection. *The American Journal of Tropical Medicine and Hygiene* **66**, 633–638.

- Meng, X.-L. and Wong, W. H. (1996). Simulating ratios of normalizing constants via a simple identity: a theoretical exploration. *Statistica Sinica* pages 831–860.
- Miller, F. D. and Abu-Raddad, L. J. (2010). Evidence of intense ongoing endemic transmission of Hepatitis C virus in Egypt. *Proceedings of the National Academy of Sciences* **107**, 14757–14762.
- Minin, V. N., Bloomquist, E. W., and Suchard, M. A. (2008). Smooth skyride through a rough skyline: Bayesian coalescent-based inference of population dynamics. *Molecular Biology and Evolution* **25**, 1459–1471.
- Murray, I., Adams, R. P., and Mackay, D. (2010). Elliptical slice sampling. *Journal of Machine Learning Research* **9**, 541–548.
- Neal, R. (2011). MCMC using Hamiltonian dynamics. *Handbook of Markov Chain Monte Carlo* **2**, 113–162.
- Opgen-Rhein, R., Fahrmeir, L., and Strimmer, K. (2005). Inference of demographic history from genealogical trees using reversible jump Markov chain Monte Carlo. *BMC Evolutionary Biology* **5**, 6.
- Pääbo, S., Poinar, H., Serre, D., Jaenicke-Després, V., Hebler, J., Rohland, N., Kuch, M., Krause, J., Vigilant, L., and Hofreiter, M. (2004). Genetic analyses from ancient DNA. *Annual Review of Genetics* **38**, 645–679.
- Paciorek, C. J. and Schervish, M. J. (2006). Spatial modelling using a new class of nonstationary covariance functions. *Environmetrics* **17**, 483–506.
- Palacios, J. A. and Minin, V. N. (2012). Integrated nested Laplace approximation for Bayesian nonparametric phylodynamics. *Proceedings of the Twenty-Eighth Conference on Uncertainty in Artificial Intelligence* pages 726–735.
- Palacios, J. A. and Minin, V. N. (2013). Gaussian process-based Bayesian nonparametric inference of population size trajectories from gene genealogies. *Biometrics* **69**, 8–18.
- Pybus, O. G., Charleston, M. A., Gupta, S., Rambaut, A., Holmes, E. C., and Harvey, P. H. (2001). The epidemic behavior of the Hepatitis C virus. *Science* **292**, 2323–2325.
- Pybus, O. G., Drummond, A. J., Nakano, T., Robertson, B. H., and Rambaut, A. (2003). The epidemiology and iatrogenic transmission of Hepatitis C virus in Egypt: a Bayesian coalescent approach. *Molecular Biology and Evolution* **20**, 381–387.
- Pybus, O. G., Rambaut, A., and Harvey, P. H. (2000). An integrated framework for the inference of viral population history from reconstructed genealogies. *Genetics* **155**, 1429–1437.
- R Core Team (2017). *R: A Language and Environment for Statistical Computing*. R Foundation for Statistical Computing, Vienna, Austria.
- Raftery, A. E., Newton, M. A., Satagopan, J. M., and Krivitsky, P. N. (2006). Estimating the integrated likelihood via posterior simulation using the harmonic mean identity. Technical Report 499, University of Washington.

- Rambaut, A., Pybus, O. G., Nelson, M. I., Viboud, C., Taubenberger, J. K., and Holmes, E. C. (2008). The genomic and epidemiological dynamics of human Influenza A virus. *Nature* **453**, 615.
- Rasmussen, D. A., Volz, E. M., and Koelle, K. (2014). Phylodynamic inference for structured epidemiological models. *PLoS Computational Biology* **10**, e1003570.
- Ray, S. C., Arthur, R. R., Carella, A., Bukh, J., and Thomas, D. L. (2000). Genetic epidemiology of Hepatitis C virus throughout Egypt. *The Journal of Infectious Diseases* **182**, 698–707.
- Reimer, P. J., Baillie, M. G., Bard, E., Bayliss, A., Beck, J. W., Blackwell, P. G., Ramsey, C. B., Buck, C. E., Burr, G. S., Edwards, R. L., et al. (2009). IntCal09 and Marine09 radiocarbon age calibration curves, 0–50,000 years cal BP. *Radiocarbon* **51**, 1111–1150.
- Reményi, N. and Vidakovic, B. (2015). Wavelet shrinkage with double Weibull prior. *Communications in Statistics-Simulation and Computation* **44**, 88–104.
- Rue, H. and Held, L. (2005). *Gaussian Markov Random Fields: Theory and Applications*. CRC Press.
- Shapiro, B., Drummond, A. J., Rambaut, A., Wilson, M. C., Matheus, P. E., Sher, A. V., Pybus, O. G., Gilbert, M. T. P., Barnes, I., Binladen, J., et al. (2004). Rise and fall of the Beringian steppe bison. *Science* **306**, 1561–1565.
- Shapiro, B., Ho, S. Y., Drummond, A. J., Suchard, M. A., Pybus, O. G., and Rambaut, A. (2010). A Bayesian phylogenetic method to estimate unknown sequence ages. *Molecular Biology and Evolution* **28**, 879–887.
- Shapiro, B. and Hofreiter, M. (2014). A paleogenomic perspective on evolution and gene function: new insights from ancient DNA. *Science* **343**, 1236573.
- Sørbye, S. H. and Rue, H. (2014). Scaling intrinsic Gaussian Markov random field priors in spatial modelling. *Spatial Statistics* **8**, 39–51.
- Stan Development Team (2017). RStan: the R interface to Stan, Version 2.14.2.
- Strimmer, K. and Pybus, O. G. (2001). Exploring the demographic history of DNA sequences using the generalized skyline plot. *Molecular Biology and Evolution* **18**, 2298–2305.
- Volz, E. and Pond, S. (2014). Phylodynamic analysis of Ebola virus in the 2014 Sierra Leone epidemic. *PLoS Currents* **6**,
- Wallin, J. and Bolin, D. (2015). Geostatistical modelling using non-Gaussian Matérn fields. *Scandinavian Journal of Statistics* **42**, 872–890.
- Yang, Z. (1994). Maximum likelihood phylogenetic estimation from DNA sequences with variable rates over sites: approximate methods. *Journal of Molecular Evolution* **39**, 306–314.
- Yang, Z. (2014). *Molecular evolution: a statistical approach*. Oxford University Press.
- Yue, Y. R., Simpson, D., Lindgren, F., and Rue, H. (2014). Bayesian adaptive smoothing splines using stochastic differential equations. *Bayesian Analysis* **9**, 397–424.

## A Discrete Approximation to Coalescent Likelihood

The integrals in equation (1) of the main text are computationally intractable since  $N_e(t)$  is an unknown infinite-dimensional parameter. However, following Palacios and Minin (2012), Gill et al. (2013), and Lan et al. (2015) we can use an approximation over a finite grid to make the computations tractable. We assume  $N_e(t) = \exp[f(t)]$ , where  $f(t)$  is a function of continuous time. We approximate  $f(t)$  by estimating it at discrete locations on a fixed grid with uniform spacing. We construct a regular grid,  $\mathbf{x} = \{x_h\}_{h=1}^H$ , and set the end points of the grid  $\mathbf{x}$  such that  $x_1 = s_m$  and  $x_H = t_1$  (see Figure 1 of main text). Now for  $t \in (x_h, x_{h+1}]$ , we have  $N_e(t) \approx \exp[\theta_h]$ , where  $\theta_h$  is an unknown model parameter. This implies that  $\boldsymbol{\theta} = \{\theta_h\}_{h=1}^{H-1}$  is a piecewise-constant approximation to  $\ln[N_e(t)]$  for  $t \in [s_m, t_1]$ .

Calculating the likelihood in equation (1) of the main text requires first sorting the combined set of time points  $\{t, s, \mathbf{x}\}$  and creating a new set of  $D = n + m + H - 4$  half-open subintervals  $\{I'_d\}_{d=1}^D$ , such that for each  $d = 1, \dots, D$  there exists an  $i, k$ , and  $h$  that satisfy  $I'_d = I_{i,k} \cap (x_h, x_{h+1}]$ . Now the integrals in equation (1) can be approximated by

$$\int_{I_{i,k}} \frac{C_{i,k}}{N_e(t)} dt \approx \sum_{I'_d \subset I_{i,k}} \frac{C_{i,k}}{\exp[\theta_h]} \Delta_d, \quad (\text{A.1})$$

where  $\Delta_d$  is the length of the subinterval  $I'_d$ . If we introduce an auxiliary variable  $z_d$  that takes the value 1 if interval  $I_d$  ends with a coalescent event ( $I'_d \subseteq I_{0,k}$ ) and 0 otherwise, then we can use equation (A.1) to write an approximation to the component of the density in equation (1) of the main text associated with interval  $(x_h, x_{h+1}]$  as

$$p(\mathbf{z}_h | s, \mathbf{n}, N_e(t)) = \prod_{I'_d \subset (x_h, x_{h+1}]} \left\{ \frac{C_{i,k}}{\exp[\theta_h]} \right\}^{z_d} \exp \left\{ -\frac{C_{i,k}}{\exp[\theta_h]} \Delta_d \right\}, \quad (\text{A.2})$$

where  $\mathbf{z}_h$  is the vector of  $z_d$  values such that  $I'_d \subset (x_h, x_{h+1}]$ . An approximation to the complete density in equation (1) is then the product of the components in equation (A.2):

$$p(t_1, \dots, t_n | s, \mathbf{n}, N_e(t)) \approx \prod_{h=1}^{H-1} p(\mathbf{z}_h | s, \mathbf{n}, N_e(t)). \quad (\text{A.3})$$

## B Setting the Global Smoothing Hyperparameter

The global smoothing parameter  $\gamma$  controls the variation in the estimated effective population size trajectory. It is therefore important to have a way to select the scale hyperparameter  $\zeta$  of the prior distribution of the global smoothing parameter that reduces subjectivity. We follow a method suggested Sørbye and Rue (2014) for intrinsic GMRF models and modified by Faulkner and Minin (2018) for SPMRF models for selecting this hyperparameter. Let  $\mathbf{Q}$  be the precision matrix for the Markov random field corresponding to the model of interest (see Faulkner and Minin (2018) for examples), and  $\boldsymbol{\Sigma} = \mathbf{Q}^{-1}$  be the covariance matrix with diagonal elements  $\Sigma_{ii}$ . The marginal standard deviation of all components of  $\boldsymbol{\theta}$  for a fixed value of  $\gamma$  is

$\sigma_\gamma(\theta_i) = \gamma\sigma_{\text{ref}}(\boldsymbol{\theta})$ , where  $\sigma_{\text{ref}}(\boldsymbol{\theta})$  is the geometric mean of the individual marginal standard deviations when  $\gamma = 1$  (Sørbye and Rue, 2014). We want to set an upper bound  $U$  on the average marginal standard deviation of  $\theta_i$ , such that  $\Pr(\sigma_\gamma(\theta_i) > U) = \alpha$ , where  $\alpha$  is some small probability (typically 0.01 to 0.05). Using the cumulative probability function for a half-Cauchy distribution, we can find a value of  $\zeta$  for a given value of  $\sigma_{\text{ref}}(\boldsymbol{\theta})$  specific to a model of interest and given common values of  $U$  and  $\alpha$  by:

$$\zeta = \frac{U}{\sigma_{\text{ref}}(\boldsymbol{\theta}) \tan\left(\frac{\pi}{2}(1 - \alpha)\right)}. \quad (\text{B.1})$$

For phylodynamic inference, we set  $U$  equal the estimated standard deviation of the log-transformed values the Skyline estimates of population size (Pybus et al., 2000) based on a fixed genealogy and set of sample times. We choose this value of  $U$  since we know that the marginal variances of the  $\theta$ s should not exceed the variance in the log-Skyline estimates, on average. For the examples in this paper, we set  $\alpha = 0.05$  as the probability of the average marginal standard deviation exceeding  $U$ .

## C Elliptical Slice within Gibbs Sampler

For models based on sequence data, we used a combination of elliptical slice sampling (Murray et al., 2010) for the latent effective population size parameters and Gibbs sampling for the latent local and global scale parameters. The Gibbs sampler was based on a modification of the approach derived by Makalic and Schmidt (2016) for Gibbs sampling of horseshoe random variables.

### C.1 Model Specifications

Using a state-space representation of the HSMRF where  $\mu$  is the fixed overall mean and  $\sigma^2$  is a fixed variance for  $\theta_1$  and  $\zeta$  is the fixed hyperparameter on the global scale, following Makalic and Schmidt (2016) the first-order HSMRF model conditional on a set of auxiliary variables can be written:

$$\begin{aligned} \mathbf{y} \mid \boldsymbol{\theta} &\sim \mathcal{L}(\mathbf{y} \mid \boldsymbol{\theta}) \\ \Delta\theta_j &\sim \mathcal{N}(0, \lambda_j^2 \eta^2 \zeta^2) \quad j = 1, \dots, n-1 \\ \theta_1 &\sim \mathcal{N}(\mu, \sigma^2) \\ \theta_i &= \theta_1 + \sum_{j=1}^{i-1} \Delta\theta_j \quad i = 2, \dots, n \\ \lambda_j^2 \mid \psi_j &\sim \text{IG}(1/2, 1/\psi_j) \\ \eta^2 \mid \xi &\sim \text{IG}(1/2, 1/\xi) \\ \psi_1, \dots, \psi_{n-1}, \xi &\sim \text{IG}(1/2, 1), \end{aligned}$$

where  $\mathbf{y}$  is the coalescent data,  $\mathcal{L}$  is the coalescent density, and  $\text{IG}$  is an inverse-gamma distribution. This formulation implies that  $\lambda_j \sim C^+(0, 1)$  and  $\eta \sim C^+(0, 1)$ . We translate this to our original model formulation by allowing the global scale parameter  $\gamma \sim C^+(0, \zeta)$ , where  $\gamma = \eta\zeta$ , and the local scale parameters  $\tau_j \sim C^+(0, \gamma)$ , where  $\tau_j = \lambda_j\gamma = \lambda_j\eta\zeta$ . This implies that  $\Delta\theta_j \sim \mathcal{N}(0, \tau_j^2)$ , which is our original way of formulating the model.

Similar to above but absent the local scale parameters, the first-order GMRF model can be written:

$$\begin{aligned}
\mathbf{y} \mid \boldsymbol{\theta} &\sim \mathcal{L}(\mathbf{y} \mid \boldsymbol{\theta}) \\
\Delta\theta_j &\sim \mathcal{N}(0, \eta^2 \zeta^2) \quad j = 1, \dots, n-1 \\
\theta_1 &\sim \mathcal{N}(\mu, \sigma^2) \\
\theta_i &= \theta_1 + \sum_{j=1}^{i-1} \Delta\theta_j \quad i = 2, \dots, n \\
\eta^2 \mid \xi &\sim \mathcal{IG}(1/2, 1/\xi) \\
\xi &\sim \mathcal{IG}(1/2, 1).
\end{aligned}$$

## C.2 Full Conditional Distributions

First we describe the full conditional distributions of the latent scale and auxiliary variables used in the Gibbs sampler for the first-order HSMRF. It can be shown that for  $j = 1, \dots, n-1$ , the full conditional distributions are:

$$\begin{aligned}
p(\lambda_j^2 \mid \cdot) &\propto \mathcal{IG}\left(1, \frac{1}{\psi_j} + \frac{\Delta\theta_j^2}{2\eta^2\zeta^2}\right) \\
p(\eta^2 \mid \cdot) &\propto \mathcal{IG}\left(\frac{n}{2}, \frac{1}{\xi} + \frac{1}{2\zeta^2} \sum_{j=1}^{n-1} \frac{\Delta\theta_j^2}{\lambda_j^2}\right) \\
p(\psi_j \mid \cdot) &\propto \mathcal{IG}\left(1, 1 + \frac{1}{\lambda_j^2}\right) \\
p(\xi \mid \cdot) &\propto \mathcal{IG}\left(1, 1 + \frac{1}{\eta^2}\right)
\end{aligned}$$

Similarly, the full conditional distributions for the scale and auxiliary variables for the first-order GMRF are:

$$\begin{aligned}
p(\eta^2 \mid \cdot) &\propto \mathcal{IG}\left(\frac{n}{2}, \frac{1}{\xi} + \frac{1}{2\zeta^2} \sum_{j=1}^{n-1} \Delta\theta_j^2\right) \\
p(\xi \mid \cdot) &\propto \mathcal{IG}\left(1, 1 + \frac{1}{\eta^2}\right)
\end{aligned}$$

## C.3 Elliptical Slice Sampling and Gibbs

We follow the algorithm in Figure 2 (pg 543) of Murray et al. (2010) for elliptical slice sampling, but with a few modifications. Suppose the elements of our observation variable  $\mathbf{y}$  are conditionally independent given a function of underlying latent Gaussian variables  $\boldsymbol{\theta} = \mathbf{f} + \boldsymbol{\mu}$ , where  $\mathbf{f} \sim \mathcal{N}(0, \boldsymbol{\Sigma})$  and  $\boldsymbol{\mu}$  is a fixed constant. We denote the likelihood of  $\mathbf{y}$  conditional on  $\boldsymbol{\theta}$  as  $\mathcal{L}(\mathbf{y} \mid \boldsymbol{\theta})$ . Following Murray et al. (2010), let  $\mathbf{f}$  be the current state of the zero-centered field parameters on the natural log scale. The algorithm proceeds by first selecting  $\boldsymbol{v} \sim \mathcal{N}(0, \boldsymbol{\Sigma})$  and drawing  $u \sim \mathcal{U}(0, 1)$ . We set the slice value  $s = \ln u + \ln \mathcal{L}(\mathbf{y} \mid \mathbf{f} + \boldsymbol{\mu})$ . We then draw a proposed angle  $\alpha \sim \mathcal{U}(0, 2\pi)$ , and define a bracket  $[\alpha_{min}, \alpha_{max}] = [\alpha - 2\pi, \alpha]$ . The current proposal is  $\mathbf{f}' = \mathbf{f} \cos \alpha + \boldsymbol{v} \sin \alpha$ . If  $\ln \mathcal{L}(\mathbf{y} \mid \mathbf{f}' + \boldsymbol{\mu}) > s$ , then we accept and set  $\mathbf{f} = \mathbf{f}'$ . Otherwise, we

shrink the bracket by setting  $\alpha_{min} = \alpha$  if  $\alpha < 0$  or setting  $\alpha_{max} = \alpha$  if  $\alpha \geq 0$ , and draw a new  $\alpha \sim \mathcal{U}(\alpha_{min}, \alpha_{max})$ . We then calculate a new proposal and keep shrinking the bracket in this manner until the proposal is accepted.

One modification we make to this process is in drawing the initial  $\mathbf{f}$  and subsequent  $\mathbf{v}$  vectors. Instead of using the multivariate normal specification, we use the state-space formulation. To do this, we first draw  $v_1 \sim \mathcal{N}(0, \sigma^2)$  and then draw  $\Delta v_j \sim \mathcal{N}(0, \lambda_j^2 \eta^2 \zeta^2)$  for  $j = 1, \dots, n - 1$  and calculate  $v_i = v_1 + \sum_{j=1}^{i-1} \Delta v_j$  for  $i = 2, \dots, n$ . Then, prior to evaluating the likelihood, we need to calculate  $\boldsymbol{\theta} = \mathbf{f} + \boldsymbol{\mu}$ . The likelihood is then  $\mathcal{L}(\boldsymbol{\theta} | \mathbf{y})$ . This approach allows us to sample the variables as multivariate normal with mean zero without needing to use the multivariate normal distribution and costly computations that come with it.

We can specify  $\boldsymbol{\mu}$  and  $\sigma^2$  using the natural log of the maximum likelihood estimates (MLE) of  $N_e(t)$  on a grid, where the coalescent times are obtained from a fixed maximum clade credibility tree, where  $\boldsymbol{\mu}$  is the log of the mean of the MLE estimates and  $\sigma^2$  is 4 times their variance. These should provide reasonable hyperparameters that will not result in too diffuse of a sampling distribution.

We use elliptical slice sampling to sample from the field parameters  $\boldsymbol{\theta}$  conditional on the latent scale parameters and use Gibbs sampling to update the latent scale parameters conditional on the field and other parameters. We alternate between these updates until convergence and the desired number of posterior samples are obtained.

## C.4 Checking Validity of Algorithms

We performed two checks of our implementation of the random field models in RevBayes. We simulated coalescent times from the four trajectories that were used in our simulations and generated genealogical trees from those times. Our first-pass check of our elliptical-slice-within-Gibbs sampler in RevBayes was to feed these trees directly into RevBayes as fixed (as in Section 3.1 of the main text) and compare the results to those obtained with our `spmr` package using Hamiltonian Monte Carlo (HMC). Trace plots for a few parameters from the RevBayes implementation indicate decent mixing (Figure S1), and plots of trends from RevBayes implementations do not show appreciable differences from those estimated using HMC with the `spmr` package (Figure S2).

We then tested our joint inference procedure in RevBayes, estimating the tree topology, coalescent times, and coalescent trajectory. To reduce computation times, we first down-sampled each tree to 100 tips, ensuring that the retained tips spanned the entire range of non-contemporaneous tips. We then simulated alignments of 500 sites using mutation rates that produced alignments with an expectation of  $\approx 0.93$  substitutions per site. Thus the simulated alignments were approximately the size of the empirical alignments and contained approximately the same amount of information (number of substitutions). For simplicity, we employed the Jukes-Cantor substitution model (with no free parameters) with no rate heterogeneity across sites. When performing the full joint analyses on these datasets, we assumed the clock rate was known (as with the Bison analysis). All tests indicated that our MCMC sampler was working correctly. The code we used for conducting these tests is available at <https://github.com/jrfaulkner/phylocode>

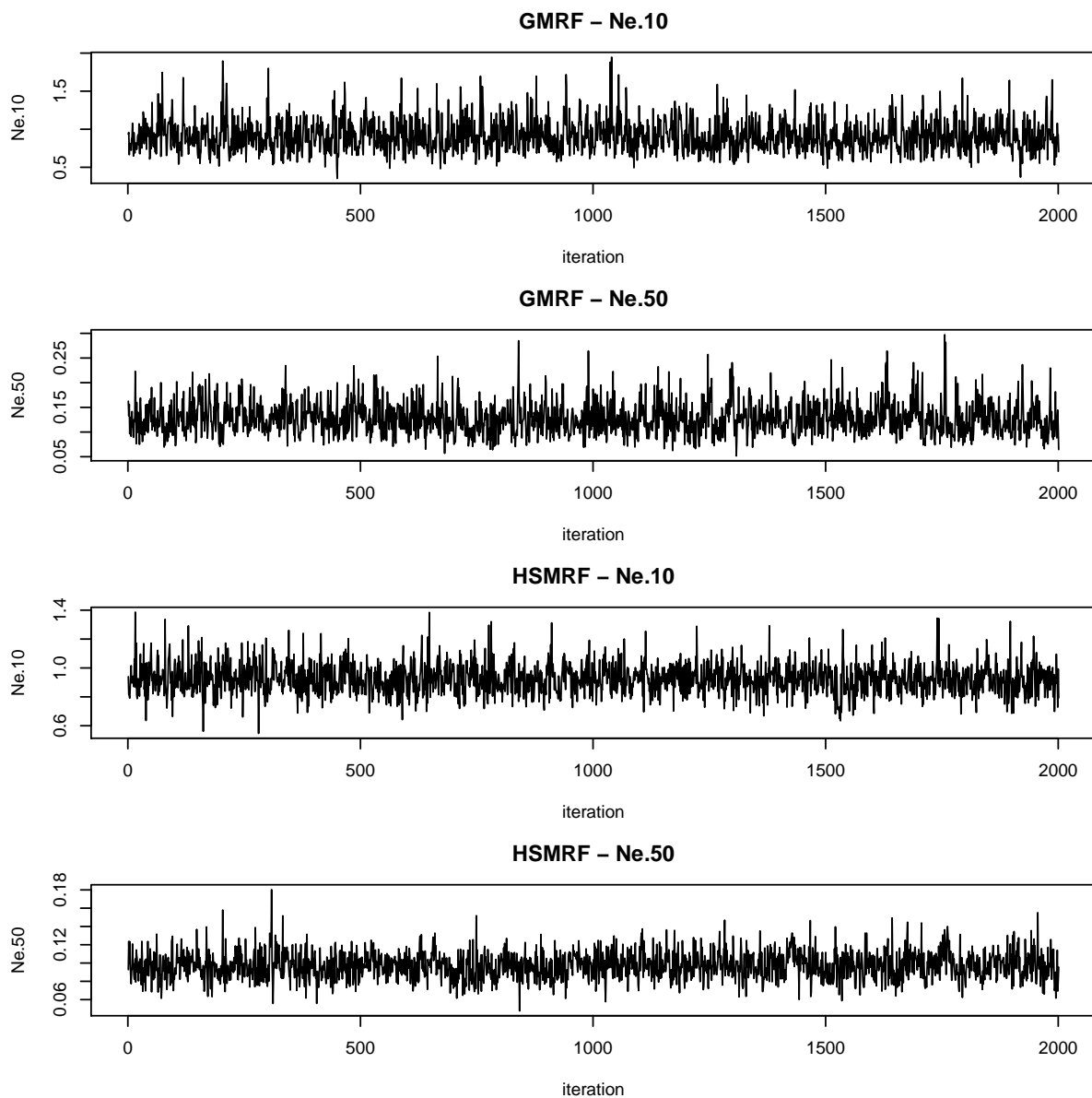


Figure C.1: Trace plots for posterior samples from two  $N_e$  parameters from models fit using our elliptical-slice-within-Gibbs sampler in RevBayes. Examples are for fixed tree coalescent data generated from the Bottleneck scenario used in the main simulations.



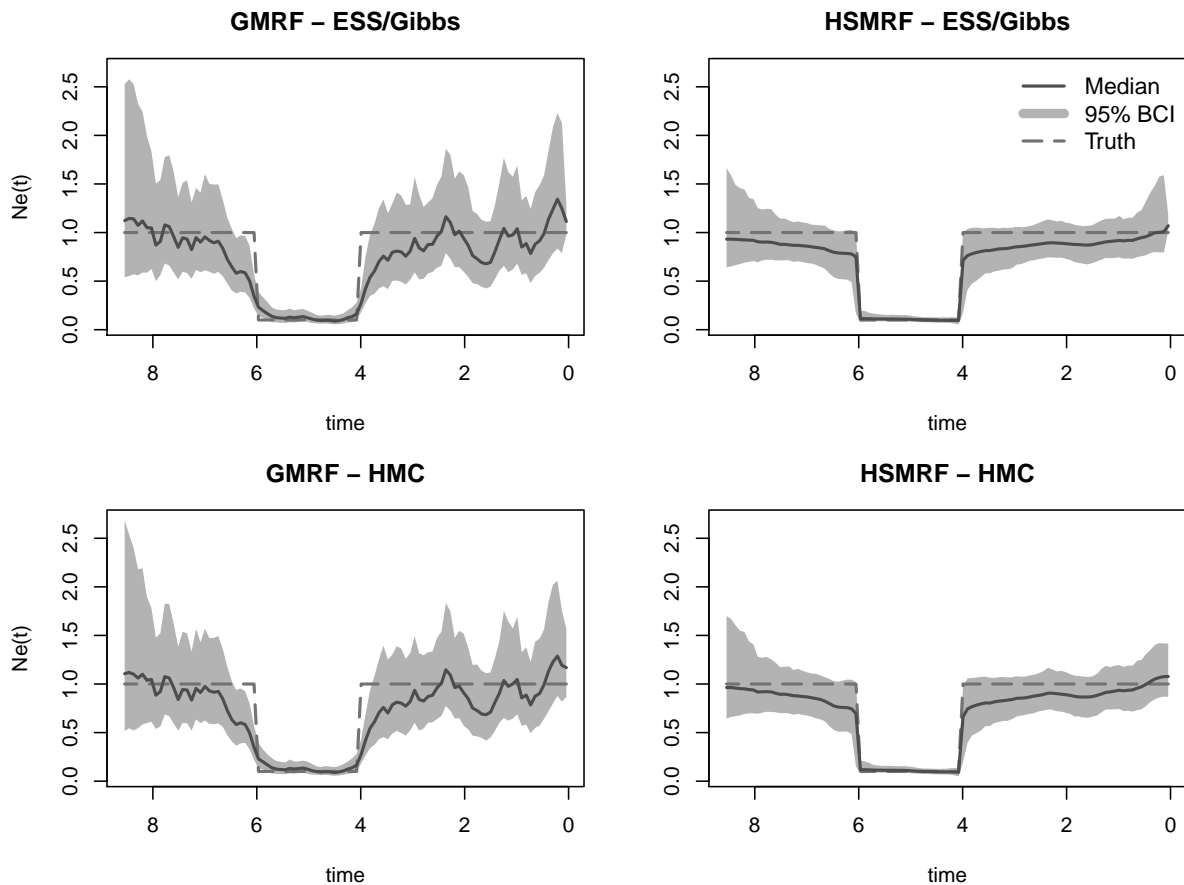


Figure C.2: Posterior medians and 95% credible intervals for  $N_e$  trajectories for two different MCMC samplers. The top row shows results from the elliptical-slice-within-Gibbs sampler in RevBayes, and the bottom shows results from the HMC sampler in Stan interfaced from the `spmr` package. Examples are for fixed tree coalescent data generated from the Bottleneck scenario used in the main simulations.

## D Simulation Details

We used simulated data to assess the performance of the HSMRF model relative to the GMRF model. We investigated four scenarios with different trajectories for  $N_e(t)$ : (1) Bottleneck (BN), (2) Boom-Bust (BB), (3) Broken Exponential (BE), and (4) Nonstationary Gaussian Process (NGP). The BN scenario had true  $N_e(t) = 0.1$  for  $4 \leq t \leq 6$  and  $N_e(t) = 1.0$  elsewhere. The BB scenario had  $N_e(t) = 0.4 + 0.25[\sin((5.5 - t)/3) + 0.75 \exp(-2.5(t - 5)^2)]$ . The BE trajectory was  $N_e(t) = \exp(-1.20 + 0.09t)$  for  $0 \leq t < 4.5$ ,  $N_e(t) = \exp(9.09 - 2.20t)$  for  $4.5 \leq t < 5$ , and  $N_e(t) = \exp(-3.57 + 0.33t)$  for  $t \geq 5$ . The trajectory for the NGP scenario, was generated from a Gaussian process with mean 0.55 and a nonstationary Matérn covariance function (Paciorek and Schervish, 2006). The covariance function was constructed so that the length scale increased rapidly in the center of the domain, resulting in a smoother  $N_e(t)$  trajectory in the center. The trajectories used for each scenario are shown at the top of Figure 2 of the main text. These effective population sizes were set to be small so the the coalescent times would be quick and would mostly fall within a time window specified for each scenario (see below).

For each scenario we generated 100 simulated data sets by first generating a random set of sampling times over a fixed interval and then generating a corresponding random set of coalescent times using the thinning algorithm proposed by Palacios and Minin (2013) and the true deterministic  $N_e(t)$  trajectories defined for each scenario. For each simulated data set, this is equivalent to assuming we know the fixed genealogical tree for a sample of DNA sequences. We found that 100 simulations per scenario was sufficient to identify meaningful differences between models without excessive computation time. We used heterochronous sampling and set the sample sizes based on the complexity of each scenario. The sample sizes were  $n = 500, 2,000, 1,000,$  and  $2,000$  and the number of lineages sampled at time zero were  $n_m = 50, 50, 100,$  and  $200$  for the BN, BB, BE, and NGP scenarios, respectively. The remaining sample times followed a uniform distribution over the domain of the sampling grid. We used a fixed grid of 101 cells where the boundary of the 100th cell was  $S$  and the final cell collected any coalescent times greater than  $S$ . The values of  $S$  were 8.5, 12, 8, and 12 for the BN, BB, BE, and NGP scenarios, respectively.

We used HMC to approximate the posterior distribution of model parameters. For each simulated data set we ran four independent chains, where each chain had 1,000 iterations of adaptation followed by 500 sampling iterations. This resulted in a total of 2,000 posterior samples. The hyperparameter on the global scale parameter was selected using the method described in Web Appendix B based on the order of the model and the observations from a single data set generated for a scenario.

## E Bison Analyses with Fixed Tree

For our analyses that assumed a fixed genealogical tree, we first had to estimate a representative tree from the sequence data. To do this, we first used the program BEAST to generate a posterior distribution of genealogical trees relating the bison specimens. We used the HKY nucleotide substitution model (Hasegawa et al., 1985) with gamma distributed rate heterogeneity, and used a Skygrid (GMRF) prior for effective population size with 100 grid cells and upper boundary of 150k years before present. Given the posterior sample of trees, we then estimated the maximum clade credibility (MCC) tree based on median node heights. The MCC tree provided a fixed set of coalescent times that were then used with the sampling times in a heterochronous likelihood to estimate effective population sizes using the posterior inference with HMC described in

Section 2.4 of the main text. We fit both first-order and second-order GMRF and HSMRF models to the fixed coalescent times.

We used Bayes factors (Kass and Raftery, 1995) and posterior model probabilities to compare evidence for different models for the fixed tree analyses only. The posterior odds of Model 1 ( $\mathcal{M}_1$ ) relative to Model 2 ( $\mathcal{M}_2$ ) conditional on the data ( $\mathcal{D}$ ) is calculated as

$$\frac{\Pr(\mathcal{M}_1 | \mathcal{D})}{\Pr(\mathcal{M}_2 | \mathcal{D})} = \frac{\Pr(\mathcal{D} | \mathcal{M}_1) \Pr(\mathcal{M}_1)}{\Pr(\mathcal{D} | \mathcal{M}_2) \Pr(\mathcal{M}_2)},$$

where  $\Pr(\mathcal{D} | \cdot)$  is the marginal (or integrated) likelihood of the data given a particular model, and the Bayes factor is the ratio of marginal likelihoods:  $B_{12} = \Pr(\mathcal{D} | \mathcal{M}_1) / \Pr(\mathcal{D} | \mathcal{M}_2)$ . For our set of four models  $\mathcal{M}_1, \dots, \mathcal{M}_4$ , we calculated the posterior probability of  $\mathcal{M}_k$  as

$$\Pr(\mathcal{M}_k | \mathcal{D}) = \alpha_k B_{k1} / \sum_{r=1}^4 \alpha_r B_{r1}$$

where  $\alpha_k = \Pr(\mathcal{M}_k) / \Pr(\mathcal{M}_1)$  is the prior odds of  $\mathcal{M}_k$  relative to  $\mathcal{M}_1$  (GMRF-1), and  $B_{11}, \dots, B_{41}$  are the Bayes factors calculated relative to  $\mathcal{M}_1$ . We assumed equal prior model probabilities, so  $B_{11} = \alpha_1 = 1$ . The marginal likelihoods used in the Bayes factors were calculated using bridge sampling (Meng and Wong, 1996) with the `bridgesampling` package (Gronau et al., 2017) in R. Calculation of marginal likelihoods typically requires many more samples than are necessary for parameter estimation, so for each model we ran four chains with 5,000 iterations of adaptation (burn-in) followed by 25,000 iterations thinned at an interval of 5, which resulted in a combined total of 20,000 posterior samples per model.

Quantitative comparison of the four models from the fixed tree analysis indicated relatively weakly positive evidence in favor of GMRF-1 and HSMRF-2. The Bayes factor comparing the marginal likelihood of HSMRF-1 relative to GMRF-1 was 0.25, the inverse of which was 4.05. The Bayes factor comparing HSMRF-2 to GMRF-2 was 13.90, with inverse 0.07. Comparing within model types, the Bayes factor for GMRF-2 vs. GMRF-1 was 0.06 (inverse 18.15), and that for HSMRF-2 vs. HSMRF-1 was 3.10 (inverse 0.32). The resulting posterior model probabilities were 0.48, 0.12, 0.03, and 0.37 for the GMRF-1, HSMRF-1, GMRF-2, and HSMRF-2 models, respectively. Using the guidelines suggested by Kass and Raftery (1995), a Bayes factor of 1 to 3 is "not worth a bare mention," of 3 to 20 is "positive," of 20 to 150 is "strong," and of  $> 150$  is "very strong." Based on these guidelines and the posterior model probabilities, one could rank the models from best to worst as GMRF-1, HSMRF-2, HSMRF-1, and GMRF-2, respectively, but strength of evidence is at best "positive" for any single model relative to another.

Qualitative visual comparison of the estimated effective population size trajectories from the four models from the fixed tree analysis indicates large differences in local behavior but general adherence to a common global trend (Figure E.1). The HSMRF-1 trajectory was less variable than the GMRF-1 on the population ascent from the past approaching the peak, but captured more complexity in the descent toward the present than the relatively straight-line descent of the GMRF-1. The HSMRF-1 indicates a slowing of decline during the LCM which the GMRF-1 does not capture, followed by a decline just after the LGM which is sharper than that shown by the GMRF-1. The results for the HSMRF-1 are similar to those for the BSKL model of Drummond et al. (2005). The GMRF-2 and HSMRF-2 models resulted in much less variable trajectories than the respective first-order models and had more clearly defined peaks. Interestingly, the HSMRF-2 results are very similar to those of the piecewise-exponential used by Shapiro et al. (2004).

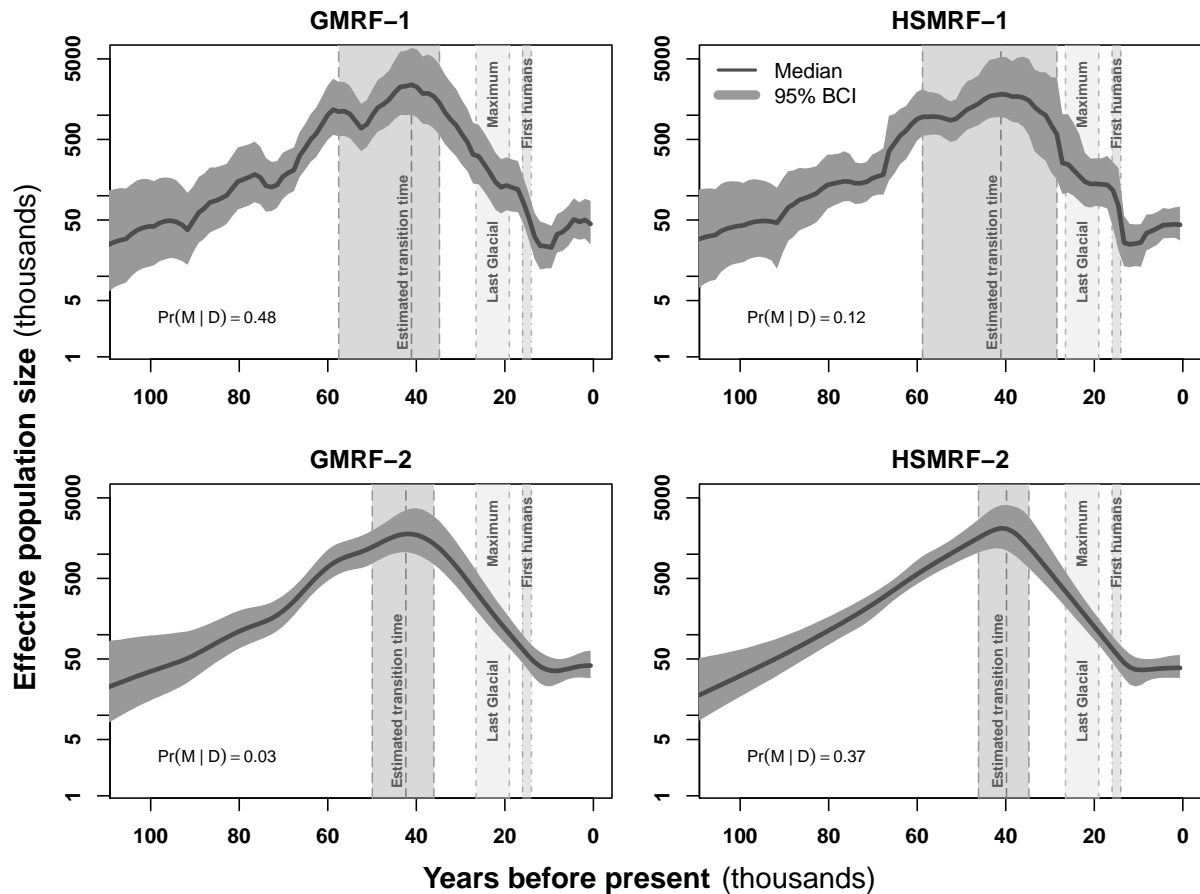


Figure E.1: Posterior medians of effective population sizes and associated 95% credible intervals for the bison data for fixed genealogies for the GMRF and HSMRF models of orders 1 and 2. Posterior median transition times (time of maximum population size) and associated 95% credible intervals and posterior model probabilities are shown for each model. The period of the Last Glacial Maximum and estimated time of first human settlement North America are shown for reference.

For these fixed tree analysis, we calculated the time of maximum population size for each posterior sample and estimated the posterior median and associated 95% credible intervals for each model (Figure E.1). These times are the estimated times of transition from population growth to population decline. Each model had similar median transition times, ranging from 39.8k years ago for the HSMRF-2 model to 42.4k years ago for the HSMRF-2 model. The credible intervals for the transition times were quite different, with the HSMRF-1 having the widest interval and the HSMRF-2 having the narrowest. It is clear from all of the models that the decline in bison population size started before the appearance of humans and before the LGM. The timing of the major decline does coincide with changes in habitat such as increased occurrence of trees and shrubs brought about by warming temperatures between 50k-35k years ago (Anderson and Lozhkin, 2001; Shapiro et al., 2004; Lorenzen et al., 2011). However, the sharp acceleration in decline around 13k to 15k years ago indicated by the GMRF-1 and HSMRF-1 models could coincide with increased hunting pressure from humans as their populations expanded.